JCB Journal of Cell Biology

ARTICLE

A modified lysosomal organelle mediates nonlytic egress of reovirus

Isabel Fernández de Castro[1], Raquel Tenorio[1], Paula Ortega-González[1], Jonathan J. Knowlton[2,3], Paula F. Zamora[2,3], Christopher H. Lee[4,5], José J. Fernández[6], Terence S. Dermody[3,4,5], and Cristina Risco[1]

Mammalian orthoreoviruses (reoviruses) are nonenveloped viruses that replicate in cytoplasmic membranous organelles called viral inclusions (VIs) where progeny virions are assembled. To better understand cellular routes of nonlytic reovirus exit, we imaged sites of virus egress in infected, nonpolarized human brain microvascular endothelial cells (HBMECs) and observed one or two distinct egress zones per cell at the basal surface. Transmission electron microscopy and 3D electron tomography (ET) of the egress zones revealed clusters of virions within membrane-bound structures, which we term membranous carriers (MCs), approaching and fusing with the plasma membrane. These virion-containing MCs emerged from larger, LAMP-1–positive membranous organelles that are morphologically compatible with lysosomes. We call these structures sorting organelles (SOs). Reovirus infection induces an increase in the number and size of lysosomes and modifies the pH of these organelles from ∼4.5–5 to ∼6.1 after recruitment to VIs and before incorporation of virions. ET of VI–SO–MC interfaces demonstrated that these compartments are connected by membrane-fusion points, through which mature virions are transported. Collectively, our results show that reovirus uses a previously undescribed, membrane-engaged, nonlytic egress mechanism and highlights a potential new target for therapeutic intervention.

Introduction

Many viruses recruit and transform membranes to facilitate viral genome synthesis and particle assembly (den Boon et al., 2010; Fernández de Castro et al., 2016). Viruses also use cell membranes for egress and cell-to-cell transmission (Altan-Bonnet, 2017; Bird and Kirkegaard, 2015). Nonenveloped viruses were thought to rely primarily on cell lysis as a means to escape infected cells. However, several nonenveloped viruses, including members of the *Parvoviridae* (Bär et al., 2008), *Picornaviridae* (Feng et al., 2013), and *Reoviridae* (Hyatt et al., 1989; Lai et al., 2013) families, use nonlytic mechanisms of egress. Nonlytic virus egress can be mediated by secretory multivesicular bodies, used by enteroviruses and hepatitis E virus (Chen et al., 2015; Nagashima et al., 2014), or secretory autophagy, used by poliovirus and rhinovirus (Bird et al., 2014; Münz, 2017). The birnavirus, infectious bursal disease virus, uses a vesicular network of unknown origin to exit cells without lysis (Méndez et al., 2017). Plant reoviruses assemble tubules formed from viral proteins and actin to facilitate nonlytic cell-to-cell virus transmission in insect vectors (Chen et al., 2017; Miyazaki et al., 2013). Rotavirus nonlytic egress occurs by a nonconventional secretion mechanism that bypasses the Golgi complex (Jourdan et al., 1998) and requires an intact actin cytoskeleton (Trejo-Cerro et al., 2017).

Mammalian orthoreoviruses (reoviruses) replicate in a wide range of cells and tissues and have been implicated in the pathogenesis of celiac disease (Bouziat et al., 2017). Reoviruses are nonenveloped, double-stranded RNA viruses that contain two concentric protein shells. Reovirus replication, transcription, and assembly occur in large cytoplasmic structures termed viral inclusions (VIs; Fernández de Castro et al., 2014). VIs are composed of membranes and recruit mitochondria (Fernández de Castro et al., 2014). Formation of VIs involves a major remodeling of ER membranes induced by the viral σNS and μNS proteins (Tenorio et al., 2018). Early steps in reovirus infection have been characterized in detail (Dermody et al., 1993; Guglielmi et al., 2006; Lai et al., 2013). However, late infection steps, such as morphogenesis of viral particles, intracellular transport, and nonlytic egress, are not well understood.

[1]Cell Structure Laboratory, National Center for Biotechnology, Spanish National Research Council, Madrid, Spain; [2]Department of Pathology, Microbiology, and Immunology, Vanderbilt University School of Medicine, Nashville, TN; [3]Department of Pediatrics, University of Pittsburgh School of Medicine, Pittsburgh, PA; [4]Department of Microbiology and Molecular Genetics, University of Pittsburgh School of Medicine, Pittsburgh, PA; [5]Center for Microbial Pathogenesis, UPMC Children's Hospital of Pittsburgh, Pittsburgh, PA; [6]Department of Macromolecular Structures, National Center for Biotechnology, Spanish National Research Council, Madrid, Spain.

Correspondence to Terence S. Dermody: terence.dermody@chp.edu; Cristina Risco: crisco@cnb.csic.es.

Reoviruses use either lytic or nonlytic egress mechanisms depending on the cell type. For example, reovirus infection of HeLa cells and Madin–Darby canine kidney cells causes lysis, whereas infection of human brain microvascular endothelial cells (HBMECs) does not (Lai et al., 2013). The autophagy pathway is a mediator of oncolytic reovirus infection in several mammalian cell types (Kemp et al., 2017), and autophagosomes facilitate nonlytic viral spread and transmission of a plant reovirus in its insect vector (Chen et al., 2017). These studies raise the possibility that an autophagic process is involved in reovirus egress.

Imaging virus egress by transmission EM (TEM) has been challenging. It is often not possible to distinguish particles entering the cell from those departing. In addition, it has been difficult to identify zones of nonlytic egress at the ultrastructural level due to their infrequent occurrence on the cell surface. To avoid these problems and unequivocally image reovirus egress, we developed a strategy based on infection with infectious subvirion particles (ISVPs). ISVPs are naturally occurring reovirus disassembly intermediates that can be obtained by proteolytic digestion of mature virions. ISVPs lack the σ3 outer-capsid protein and therefore can be distinguished from fully formed, mature progeny particles. We infected HBMECs with either intact virions or ISVPs and localized reovirus egress zones based on the presence of newly formed σ3 encapsidated onto nascent viral particles. We consistently observed one or two egress zones per cell and imaged those sites by 2D and 3D TEM. We discovered that lysosomes are redistributed during infection and collect mature virions from VIs. The modified lysosomes become filled with progeny virions that are attached to filaments. Smaller membranous organelles emerge from the virion-filled modified lysosomes and transport mature virions to the plasma membrane for egress. These results unveil a new means by which viruses exit host cells.

Results

Reovirus is released from endothelial cells in membrane-enclosed packets

To study reovirus egress, we developed an imaging-based strategy to distinguish reovirus progeny from particles entering cells (Fig. 1). First, we examined cells for structures associated with virus entry. HBMECs were infected with reovirus for 4 h, processed using nonpermeabilizing conditions, and imaged using immunofluorescence and confocal microscopy (Fig. 1 A) or TEM (Fig. 1 B). Confocal microscopy showed single viral particles as fluorescent puncta likely on the cell surface (Fig. 1 A). TEM showed single viral particles attached to the plasma membrane, associated with clathrin-coated pits, and inside small intracellular vesicles, characteristic of receptor-mediated endocytosis (Fig. 1 B; Maginnis et al., 2008).

To visualize reovirus egress, cells were infected with ISVPs (Fig. 1 C), which were produced by digestion of purified, mature virions with chymotrypsin. Virion-to-ISVP conversion was confirmed by SDS-PAGE, which demonstrated loss of the σ3 outer-capsid protein (Fig. 1 D). To determine the optimum time after infection to study reovirus egress, we defined the kinetics of reovirus replication following infection with ISVPs (Fig. 1 E). After 18 h postinfection (hpi), progeny particles were detected in high titer in the culture supernatant. ISVPs used for infection do not contain σ3, which is a capsid constituent of newly formed viral progeny. Thus, detection of σ3 by immunofluorescence at 18 hpi revealed progeny viruses exiting infected cells (Fig. 1 F). Confocal microscopy showed σ3 fluorescent signal in discrete zones at the basal surface (Fig. 1 F). We examined 50 cells and observed from one to four egress zones per cell with an average of 1.72. Anti-σ3 monoclonal antibody 10C1 did not label VIs (Fig. 1 F), whereas anti-σ3 antiserum VU219 and anti-σ3 monoclonal antibody 8H1 labeled σ3 only at the VI periphery. We conclude that σ3 epitopes must be partly masked inside VIs and that anti-σ3 antibodies do not bind virions inside these structures. EM of these zones showed release of progeny virions from single-membrane organelles that we term membranous carriers (MCs; Fig. 1 G). MCs are spherical structures of ∼0.5–1 µm in diameter and contain electron-dense material and mature virions.

We next examined the 3D structure of reovirus egress zones using single- and double-tilt electron tomography (ET; Fig. 2). In these zones, MCs very close to the plasma membrane contained membranous channels with attached virions (Figs. 2, A and B). Viral particles displayed pentagonal or hexagonal contours, consistent with icosahedral symmetry, and are bound to filaments (white arrows in Fig. 2 B). The tomographic volumes showed MCs close to or in contact with the plasma membrane (Fig. 2 C). Prior to egress, virions appear bound to membranous channels inside MCs (Fig. 2 C, reconstruction on the left). In egress areas, there were numerous virions inside MCs bound to filaments along with virions that appear to be in the act of release (Fig. 2 C, image on the right; and Video 1). Thus, reovirus particles egress in large numbers through distinct egress zones by fusion of virion-filled MCs with the plasma membrane.

Transport of virions from VIs to MCs is mediated by a lysosome-like organelle

After establishing that reovirus exits endothelial cells in membrane-enclosed packets, we studied the biogenesis of these structures. Considering that progeny virions assemble in VIs, we imaged the periphery of these reovirus-induced neoorganelles. We observed the formation of large structures distinct from MCs with a diameter of several microns filled with membranes and viral particles (Fig. 3). Interestingly, although VIs contain both mature and empty virions, most viral particles inside the large membranous structures are mature virions. We call these structures sorting organelles (SOs; Fig. 3 A). Higher magnification views of the VI–SO interface revealed that although the VI periphery has both mature virions and empty viral particles, the SOs contain only mature virions (Fig. 3 B). Enlarged images of intact VIs showed that virions are frequently attached to filaments (Fig. S1 A and insets). In infected cells, many mature virions inside VIs and SOs were attached to filaments (79.6% and 84.4%, respectively), while few empty viral particles had filaments attached (13.6% and 0%, respectively; Fig. S1 B).

At the VI periphery, we observed that SOs appear to exist in different stages (Fig. 3 C). SOs with few viral particles morphologically

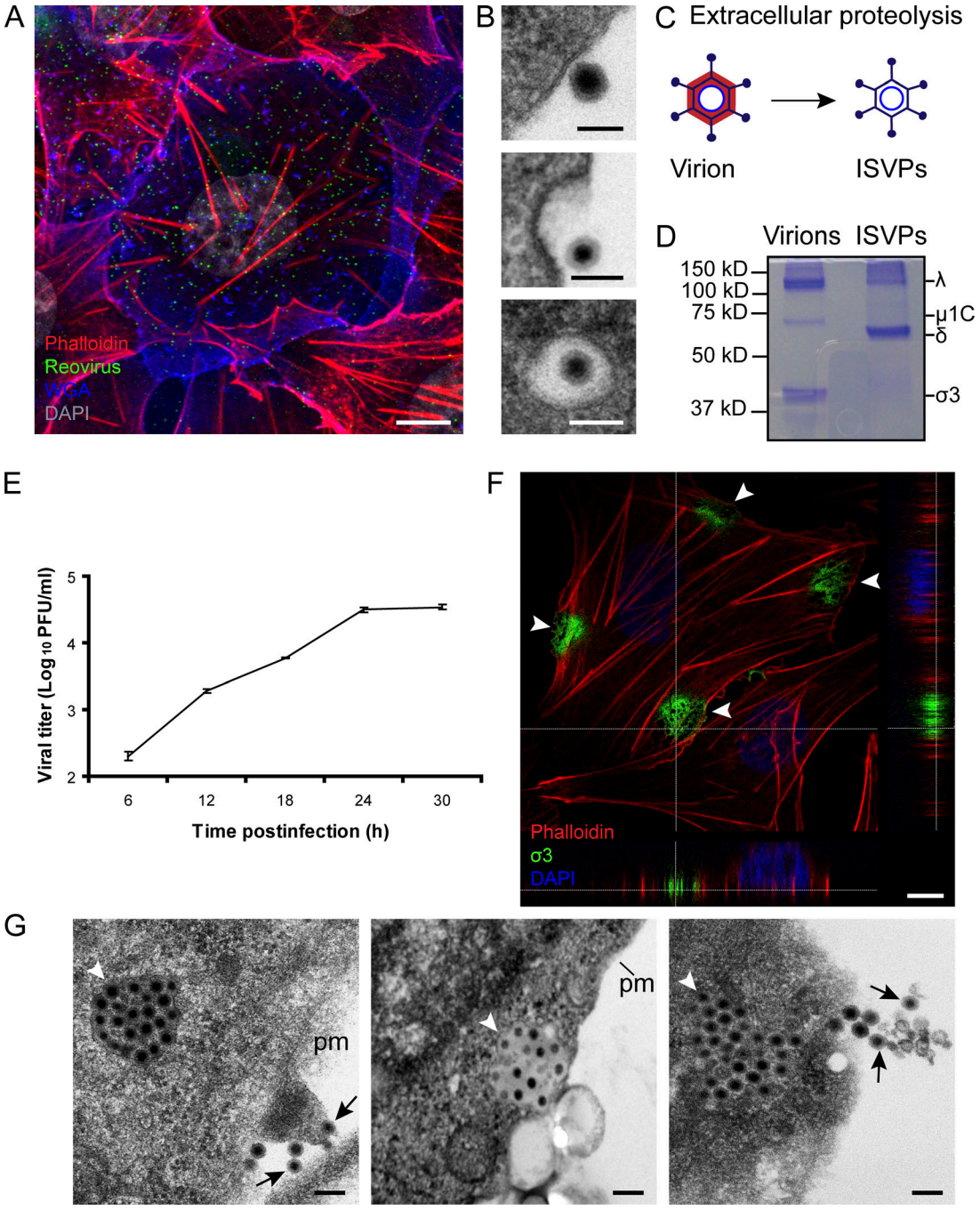

Figure 1. **Visualizing reovirus entry and egress in HBMECs using confocal microscopy and EM. (A)** HBMECs were adsorbed with reovirus T1L M1-P208S at an MOI of 20 PFUs/cell and imaged by confocal immunofluorescence microscopy without cell permeabilization at 4 hpi. Virus (green) was labeled with a reovirus-specific antiserum, actin (red) was labeled with phalloidin, and WGA (blue) was used to label the plasma membrane. Nuclei are labeled in gray. Reovirus particles are observed in a punctate pattern on the cell surface. Scale bars, 10 µm. **(B)** EM of ultrathin sections of infected cells processed by high-pressure freezing and freeze substitution. The images show reovirus attachment and internalization into organelles compatible with endosomes. Scale bars, 100 nm. **(C)** Reovirus ISVPs were prepared by digestion of purified virions with chymotrypsin. **(D)** SDS-PAGE shows that ISVPs lack the σ3 capsid protein and contain the δ cleavage product of µ1C protein. **(E)** Viral titers following adsorption of HBMECs with reovirus ISVPs at an MOI of 1 PFU/cell. **(F)** Cells were adsorbed with reovirus ISVPs, fixed 18 hpi, permeabilized, and imaged by confocal immunofluorescence microscopy following staining with anti-σ3 mouse monoclonal antibody 10C1. Fluorescent signal concentrates in discrete zones at the basal surface are shown in the confocal total projection and lateral merged image. Scale bar, 10 µm. **(G)** EM of basal surfaces of infected HBMECs adsorbed with ISVPs shows reovirus egress zones. Arrowheads point to virion-containing MCs, which are close to plasma membrane (pm) and releasing virions (arrows). Representative images from 100 cells obtained in six independent experiments are shown. Scale bars, 200 nm.

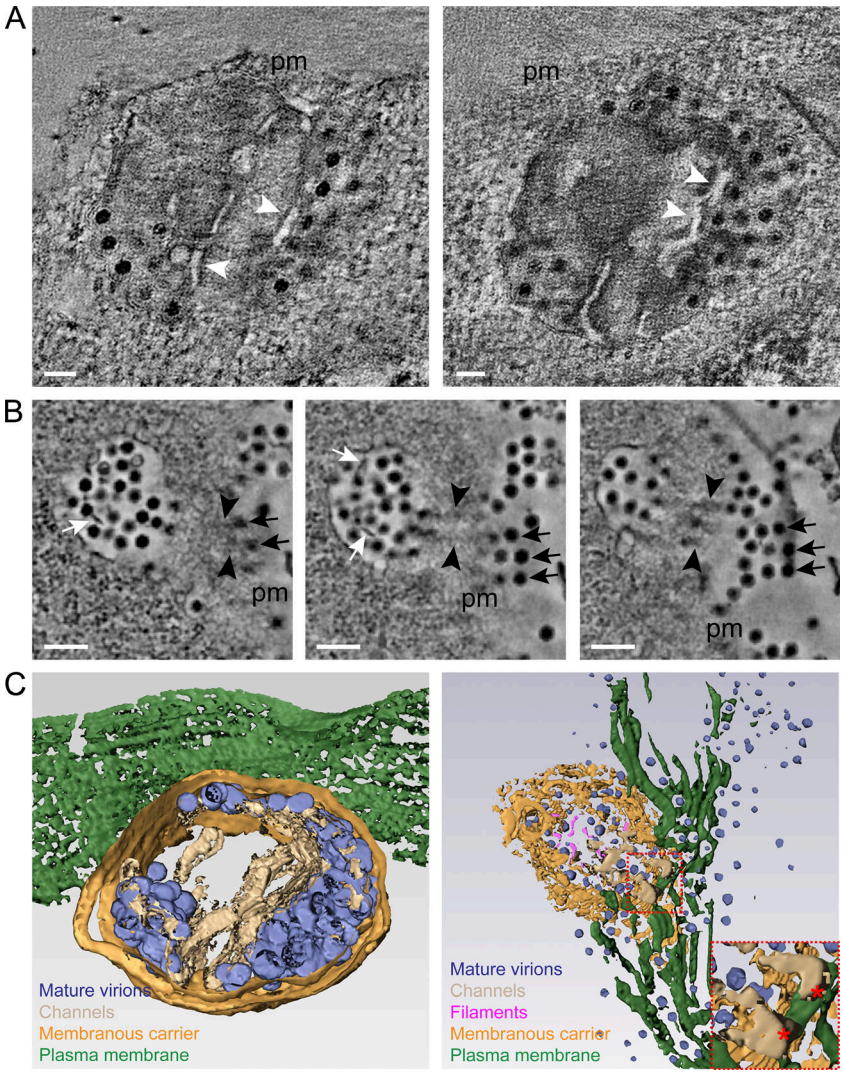

Figure 2. **ET of reovirus egress zones.** HBMECs were adsorbed with reovirus T1L M1-P208S at an MOI of 1 PFU/cell and processed at 18 hpi by high-pressure freezing, freeze-substitution, semithick sectioning, and TEM. **(A and B)** Double-tilt tomography. **(A)** Computational tomographic slices showing an MC close to the plasma membrane (pm) with membranous channels (white arrowheads) and virions. **(B)** An MC contacting the plasma membrane in which virions are attached to filaments (white arrows). Viral particles associate with membranous channels (black arrowheads) in the MC–plasma membrane interface. Virions released to the extracellular medium are labeled with black arrows. **(C)** 3D reconstructions of reovirus egress zones. Left: An MC (gold) with membranous channels (beige) and virions (blue). The plasma membrane is colored in green. Right: An MC loaded with virions (blue) is observed to contact and fuse with the plasma membrane (green). Virions inside the MC are bound to filaments (pink). The dashed red box marks the fusion between the MC channels and the plasma membrane. The inset is an enlarged image of the fusion zone between the MC and the plasma membrane. Asterisks mark the membranous channels contacting the plasma membrane. Scale bars, 200 nm. A tomogram movie is presented in Video 1.

resembled lysosomes or autolysosomes (Fig. 3 C, left and middle). SOs with many particles occasionally were associated with smaller membrane-bound, virion-containing structures that appeared to be budding from the larger structures (Fig. 3 C, right). The morphology and dimensions of the smaller structures budding from SOs resembled MCs (compare Fig. 3 C, image on the right, with Fig. 1 G). Therefore, SOs appear to collect mature virions on the periphery of VIs, and smaller virion-containing MCs form by budding from SOs. Quantification of mature virions and empty viral particles in VIs, SOs, and MCs from 25 cells supports the conclusion that SOs and MCs contain mostly mature virions (Fig. 3 D).

Characterization of SO modified lysosomes

To elucidate the composition of SOs, we labeled infected cells with markers of intracellular compartments and conducted imaging studies using confocal microscopy and correlative light and EM (CLEM; Fig. 4). HBMECs cultured on photoetched gridded coverslips were infected with reovirus, labeled with the lysosome marker LysoTracker, and imaged using fluorescence microscopy (Fig. 4 A, image on the left). Phase-contrast microscopy identified VIs as dark globular or elongated structures (asterisks in Fig. 4 A, left). Globular organelles labeled with LysoTracker are distributed adjacent to VIs (Fig. 4 A). CLEM of selected cells confirmed that these globular organelles labeled with LysoTracker are SOs containing mature virions (Fig. 4 A, middle and right). In contrast, markers for both autophagosomes and autophagolysosomes (LC3 and monodansylcadaverine) did not label SOs (data not shown). During reovirus infection, there were changes in the size, number, and distribution of lysosomes labeled with LysoTracker (Fig. 4 B). In infected cells, LysoTracker-positive organelles are recruited to the perinuclear VIs and enlarge (arrows in Fig. 4 B). To determine how the distribution of lysosomes changes during reovirus infection, we visualized mock- and reovirus-infected cells labeled with LysoTracker using live-cell microscopy (Videos 2, 3, 4, and 5). In mock-infected cells, lysosomes were concentrated in the perinuclear region and appear to distribute diffusely (Video 2). In reovirus-infected cells, VIs were identified by phase-contrast microscopy as dark, globular structures. Lysosomes move to and concentrate near VIs, virtually surrounding these replication organelles (Video 3). Higher-resolution movies of reovirus-infected cells showed additional details, such as fusion of lysosomes near VIs (Video 4). Smaller, LysoTracker-containing

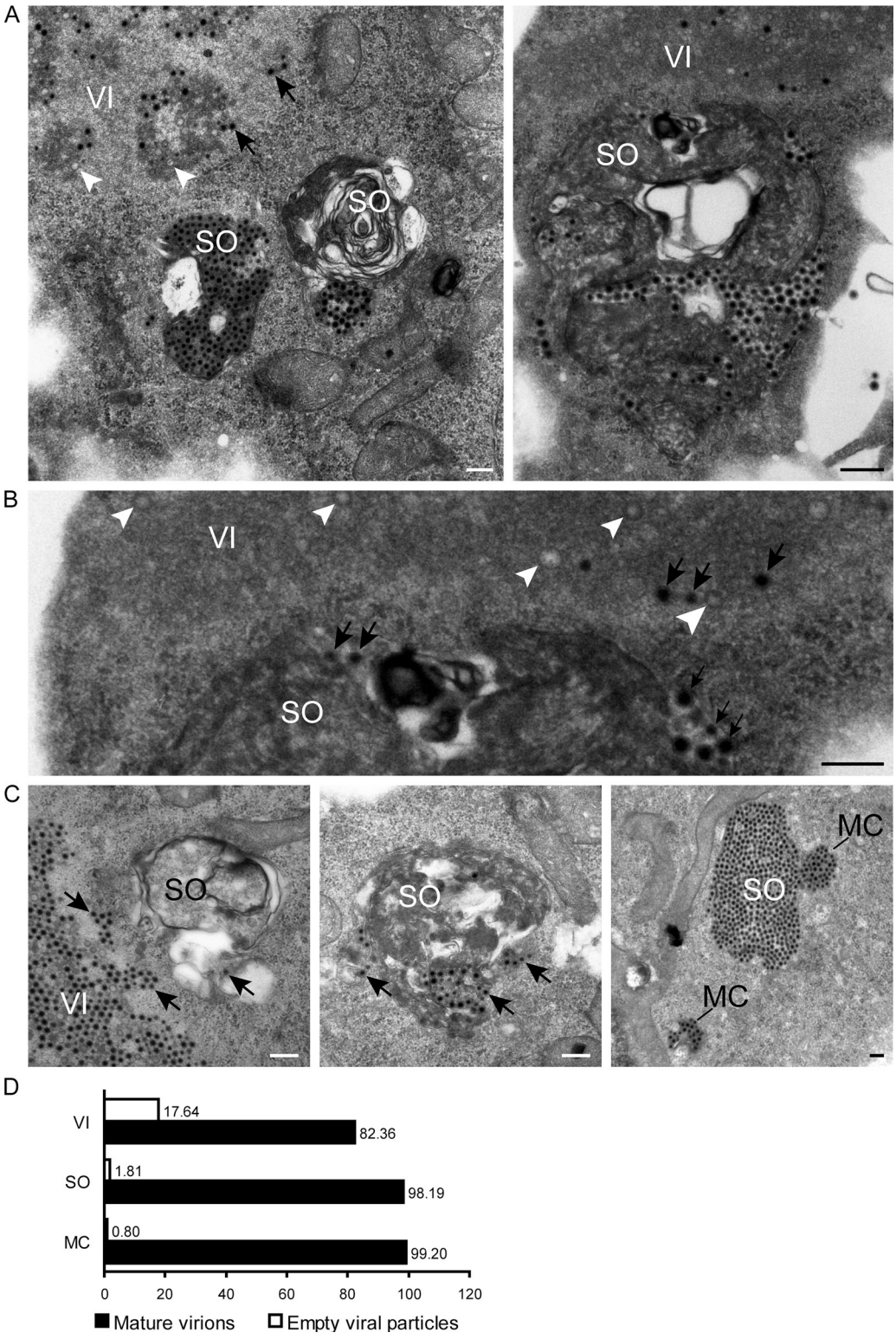

Figure 3. **Ultrastructure of SOs in cells processed by high-pressure freezing and freeze-substitution.** HBMECs were adsorbed with reovirus T1L M1-P208S at an MOI of 1 PFU/cell and imaged by EM at 18 hpi. **(A)** Ultrathin section showing a VI with mature virions (arrows) and empty viral particles (arrowheads). Two SOs with mature virions and lamellae are apparent near the VI. Scale bar, 500 nm. A higher magnification of an SO from a different cell is shown in the panel on the right. Mature virions and membranes fill the SO, while empty viral particles are only seen in the VI. Scale bar, 200 nm. **(B)** Enlarged image of the VI–SO interface from the cell shown in A on the right. Empty particles (arrowheads) and mature virions (arrows) are detected at the VI periphery in apposition with the SO, which exclusively contains mature virions. Scale bar, 200 nm. **(C)** Maturation stages of SOs. The image on the left shows an SO near a VI incorporating mature virions (arrows). An SO with dense, membranous content and virions is apparent in the center image. The image on the right shows an SO with many virions and an adjacent MC. MCs are electron dense and contain tightly packed virions. Scale bars, 200 nm. **(D)** The percentage of mature virions and empty viral particles present in VIs, SOs, and MCs. Data are presented as absolute values from 25 cells with a total of 23 VIs, 10 SOs, and 7 MCs.

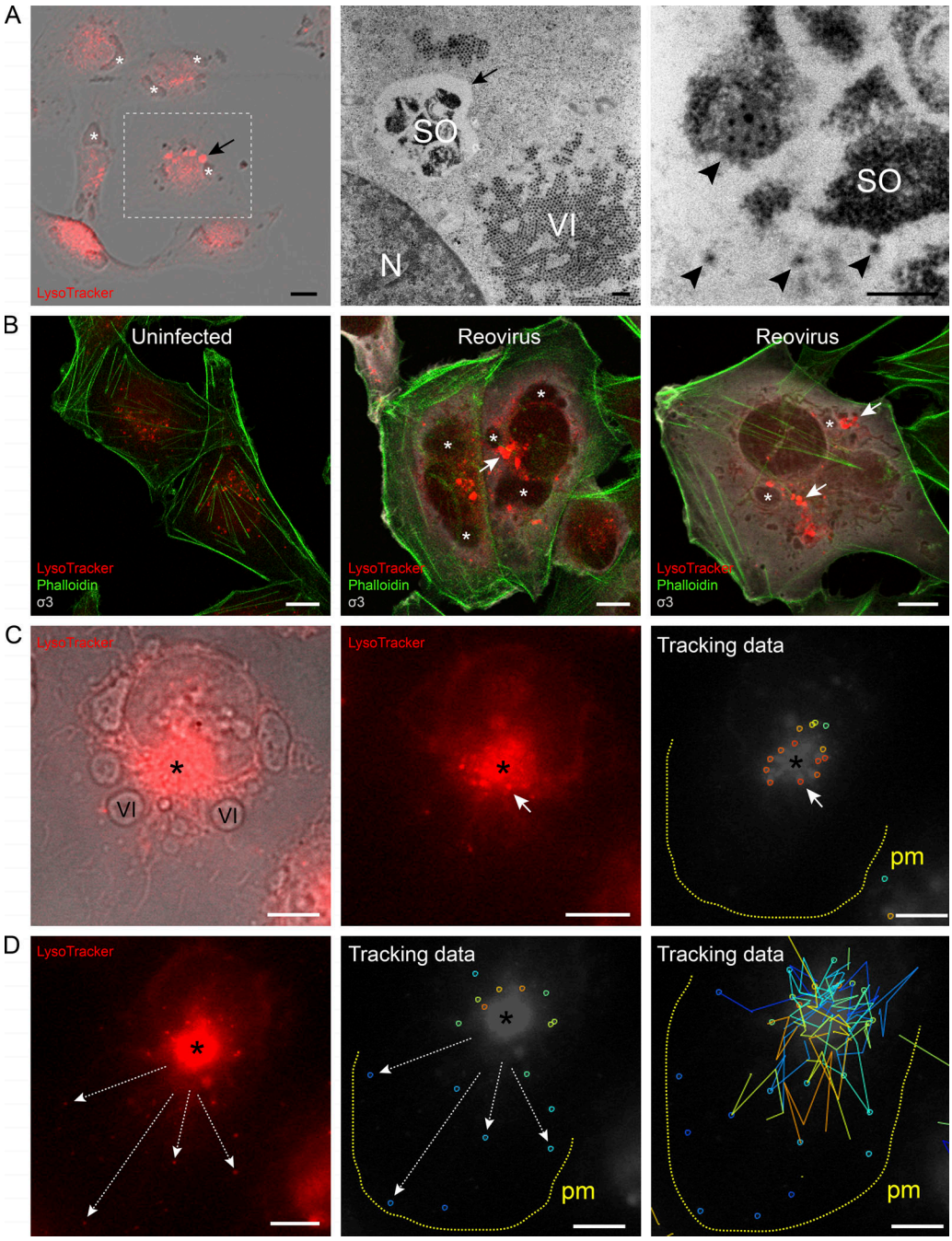

Figure 4. **CLEM and confocal microscopy of SOs.** HBMECs were either mock infected or adsorbed with reovirus T1L M1-P208S at an MOI of 1 PFU/cell and processed at 18 hpi for CLEM and confocal microscopy. **(A)** CLEM of infected HBMECs. The image on the left shows phase-contrast and fluorescence micrographs of infected cells stained with LysoTracker (red). The white dashed box marks the cell selected for EM; the black arrow indicates a lysosome close to a VI (white asterisks). Scale bar, 10 µm. Panels on the right show EM images of the selected cell. The arrow indicates the lysosome near a VI and the nucleus (N) observed in the previous image. This lysosome is an SO, as confirmed in the enlarged image of the third panel showing virions inside the SO (arrowheads). Scale bars, 500 nm. **(B)** Confocal immunofluorescence images of mock- and reovirus-infected HBMECs stained with phalloidin (green), LysoTracker (red), and an antiserum specific for σ3 (rabbit VU219). Arrows indicate lysosomes/SOs close to VIs, which are marked with asterisks. Scale bars, 10 µm. Live-cell imaging of lysosomes in uninfected and reovirus-infected cells are shown in Videos 2, 3, 4, and 5. **(C and D)** Tracking of lysosomes recruited to VIs in the same cell. Panels on the left and middle show single images of a live-cell microscopy video. The phase-contrast and fluorescence images show an infected cell stained with LysoTracker (red). Lysosomes adjacent to VIs are labeled by dark asterisks. The tracking data obtained with the TrackMate plugin of ImageJ-Fiji software are shown in the images on the right panel of C and right and middle panels of D. The specific trajectory of some lysosomes, most likely MCs (small colored circles), is marked by white arrows in D. Some lysosomes are first observed adjacent to VIs and then move to the plasma membrane (yellow dashed line, pm). Automatic tracks (marked with different colors) are shown in the right panel of D. A time-lapse recording is provided in Video 5. Scale bars, 10 µm.

structures emerge and radiate peripherally on filament tracks to the plasma membrane from the region populated with lysosomes and VIs (Video 5).

To study the lysosomal movement shown by live-cell imaging from VIs to the cell periphery, we analyzed individual lysosomes using TrackMate single-particle tracking software (Figs. 4, C and D). Phase-contrast and time-lapse microscopy images depicted the infected cell with an accumulation of lysosomes and VIs, corresponding to an early stage of lysosome recruitment (Fig. 4 C). The migration of some lysosomes at a late stage of the process is shown in Fig. 4 D. Using the TrackMate plugin (Tinevez et al., 2017), individual lysosomes were tracked (Fig. 4, C and D, panels on the right, and Fig. 4 D, middle panel). The migration tool of ImageJ-Fiji software (Schindelin et al., 2012) was used to produce traces for each lysosome. The full traces were filtered to remove static lysosomes by applying a threshold of at least 10 µm in total displacement. A total of seven of nine lysosomes (77%) analyzed in the cell shown migrated toward the plasma membrane (arrows in Fig. 4, C and D, right panels, and Fig. 4 D, middle panel). In contrast, in uninfected cells (Video 2), lysosomes distributed diffusely throughout the cytoplasm (tracking data not shown).

To determine whether SOs contain markers for lysosomes, we stained infected cells using an antibody specific for LAMP-1 (Fig. 5). Confocal microscopy of uninfected and reovirus-infected cells demonstrated a reorganization of LAMP-1–positive, reovirus σ1–positive organelles around VIs during infection (Fig. 5 A). Using Imaris software, we observed in 3D reconstructions both LAMP-1 and σ1 protein signals grouped near VIs (dashed boxes in Fig. 5 A, right panel). Varying views of the 3D model demonstrating the distribution of LAMP-1 and σ1 signals across the cell are shown in Video 6. To more precisely visualize the intracellular distribution of both proteins, we used superresolution stimulated emission depletion (STED) microscopy. LAMP-1 and σ1 signals were observed in a perinuclear region close to inclusions (Fig. 5 B). Analysis of this zone by STED revealed a clear colocalization of both protein signals (left panels). We quantified the distribution of LAMP-1–positive structures in a total of 50 regions of interest in uninfected and reovirus-infected cells (Fig. 5 C). This analysis revealed significant differences in lysosomal distribution in uninfected and reovirus-infected cells. In contrast to uninfected cells, lysosomes were mostly distributed in the perinuclear region in infected cells (<5 µm from the nuclear rim), and very few lysosomes were observed in distal regions (>15 µm from the nuclear rim; Fig. 5 D). These results demonstrate that lysosome distribution and movement are altered by reovirus infection. Double-immunogold labeling of thawed cryosections showed colocalization of LAMP-1 (10 nm gold) and σ3 (5 nm gold) in SOs containing mature virions (Fig. 6 A, left). Lysosomal marker LAMP-1 also was found in virus-filled MCs (Fig. 6 A, right). Additional examples of an SO and some MCs labeled with LAMP-1 antibody are shown in Fig. S1, C and D. These findings suggest that reovirus uses modified lysosomes to facilitate egress of progeny viral particles from VIs to the cell periphery.

To study how lysosomes are modified by reovirus infection, we determined the number and size of these organelles in uninfected and reovirus-infected cells. HBMECs were either mock infected or adsorbed with reovirus strain type 3 Dearing (T3D) at an MOI of 1 plaque-forming unit (PFU)/cell. At 18 hpi, immunofluorescence staining with mouse monoclonal antibody 9GB5 specific for T3D σ1 protein confirmed that all cells in the monolayer were infected (data not shown). Lysosomes were labeled with anti-LAMP-1 as described, and cells were imaged using confocal microscopy to analyze individual and aggregated lysosomes based on area (Fig. S2). Representative examples of the confocal and segmented images obtained from uninfected and reovirus-infected cells used for quantification are shown in Fig. S2 A. From the segmentation of the lysosomes present in each confocal image, the number and area of each can be calculated. Using the area measurements, we established criteria to classify lysosomes as individual (area <0.78 μm^2) and aggregated (area ≥0.78 μm^2), as determined by the standard size of lysosomes (0.1–1 µm; Xu and Ren, 2015). We found that reovirus infection was associated with a significant increase in the total number of lysosomes (Fig. S2 B, left panel), including both individual and aggregated lysosomes (Fig. S2 B, center and right panels). Additionally, reovirus infection was associated with a significant increase in the size of individual and aggregated lysosomes (Fig. S2 C). Therefore, these results demonstrate that reovirus infection induces an increase in the number and size of lysosomes.

Under physiological conditions, the interior of lysosomes is acidic with a pH of 4.5–5.0 (Geisow, 1984, Maxfield, 2014). Lysosomal enzymes are acid hydrolases that are active at this pH (Mindell, 2012). Therefore, the regulation of lysosomal pH is essential for lysosomal function, and pH elevations can impede the activity of lysosomal enzymes. Since reovirus particles would be degraded by active lysosomal enzymes, we assessed the luminal pH of individual lysosomes and SOs in uninfected and reovirus-infected cells using quantitative fluorescence microscopy. Mock-infected or reovirus-infected HBMECs were incubated with FITC and rhodamine probes coupled to dextrans. The FITC/rhodamine ratio is higher at neutral pH and lower at acidic pH. Using a calibration curve, pH values were determined by extrapolation of ratio values (Meo-Evoli et al., 2015). The average pH value for the bulk of acidic compartments in uninfected and reovirus-infected cells was 6.98 and 6.69, respectively, with no significant differences between these two values.

To calculate the pH of the lysosome-like organelles adjacent to VIs, we quantified the FITC/rhodamine ratio of >100 single organelles on the periphery of VIs, as shown in Fig. S3 A. The pH of large organelles attached to VIs, most likely SOs, is 6.1. This value differs significantly from the pH of bulk acidic organelles in infected cells (Fig. S3 B) and is higher than the pH of functional lysosomes (pH 4.5–5). Interestingly, lysosome luminal pH is not homogeneous. In uninfected cells, peripheral lysosomes are less acidic than juxtanuclear ones despite their comparable buffering capacity (Johnson et al., 2016). Immunofluorescence with an anti-σ1 antibody showed that lysosomes recruited to VIs, either with or without virions contained within, have a pH of ∼6.1, higher than the pH of perinuclear lysosomes in uninfected cells (Fig. S3 C). In immunofluorescence experiments using a mouse monoclonal antibody specific for cathepsin B (Calbiochem; CA10), we observed labeling of lysosomes, but not SOs

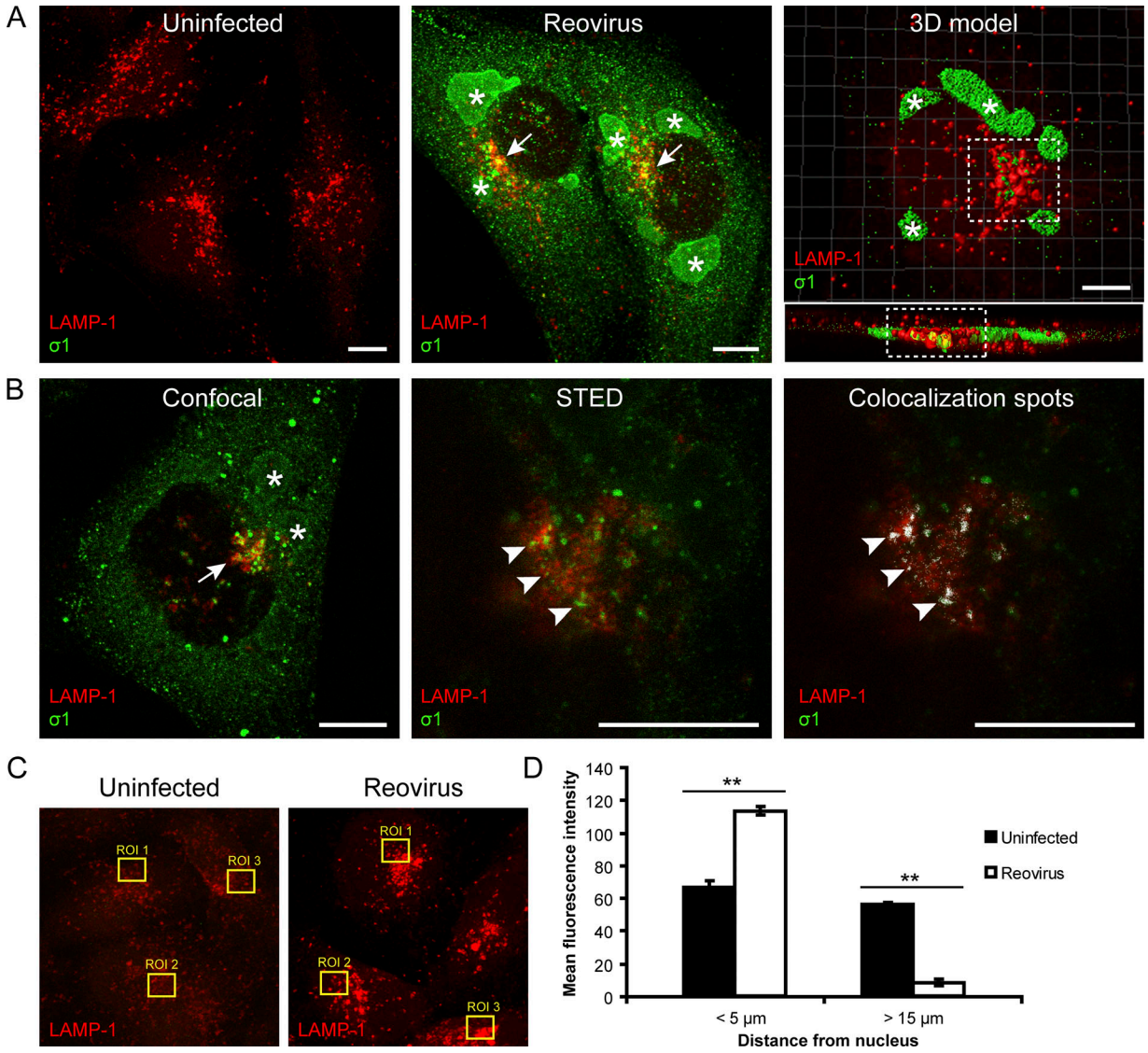

Figure 5. **Redistribution of lysosomes during reovirus infection.** HBMECs were either mock-infected or adsorbed with reovirus strain T3D at an MOI of 1 PFU/cell and processed at 18 hpi for confocal and superresolution STED microscopy. Immunofluorescence experiments were conducted using antibodies specific for LAMP-1 (red) and σ1 (mouse monoclonal antibody 9GB5 specific for T3D σ1, green). **(A)** Confocal micrographs showing lysosomes/SOs (arrows) close to VIs (asterisks). A 3D reconstruction from a series of confocal images is shown on the right. Dashed boxes mark areas in which the LAMP-1 and σ1 signals concentrate in the frontal and lateral projections of the volume. A 3D model is provided in Video 6. **(B)** Confocal and STED microscopy of a reovirus-infected cell showing association of LAMP-1 and σ1 near VIs (arrow and arrowheads, respectively). High-resolution STED microscopy also showed some sites of colocalization (image on the right). **(C and D)** Quantification of lysosome distribution in uninfected and infected cells is shown as the mean total fluorescence signal intensity detected at <5 µm or >15 µm from the nuclear rim. Fifty regions of interest were selected using LAS X software (Leica Microsystems). Three representative examples are shown in the left panels. The results are presented as mean fluorescence intensities of LAMP-1 ± SEM (n = 50 regions of interest). **, P < 0.01, unpaired, two-tailed Student's t test. Scale bars, 10 µm.

recruited to VIs (data not shown). A negative immunolabeling result is not conclusive. However, if proteases are retained inside SOs containing virions, then these enzymes likely would not be functional, as the luminal pH of SOs is 6.1 (Fig. S3) and the optimal pH of lysosomal proteases is 4.5–5.0.

Reorganization of lysosomes is a general characteristic of reovirus infection

To determine whether the observed recruitment and use of lysosomes is a general feature of reovirus infection, we imaged lysosomes in different cell types infected with reovirus. In reovirus-infected HeLa cells and Vero cells, LAMP-1–positive lysosomes were recruited to VIs (Fig. S4, A and B). In these cell lines, SOs with mature virions also appeared adjacent to VIs by TEM (Fig. S4 C). To test whether lysosome reorganization is induced by different reoviruses, we infected cells with different reovirus strains (Fig. S4, D–G). Confocal microscopy images of HBMECs infected with strains type 1 Lang (T1L) or T3D showed that lysosomes labeled with anti-LAMP-1 antibody were recruited to VIs (Fig. S4 D). The reovirus σ1 capsid protein associated with LAMP-1 in discrete areas near inclusions (Fig. S4 D). Moreover, SOs and MCs containing mature virions

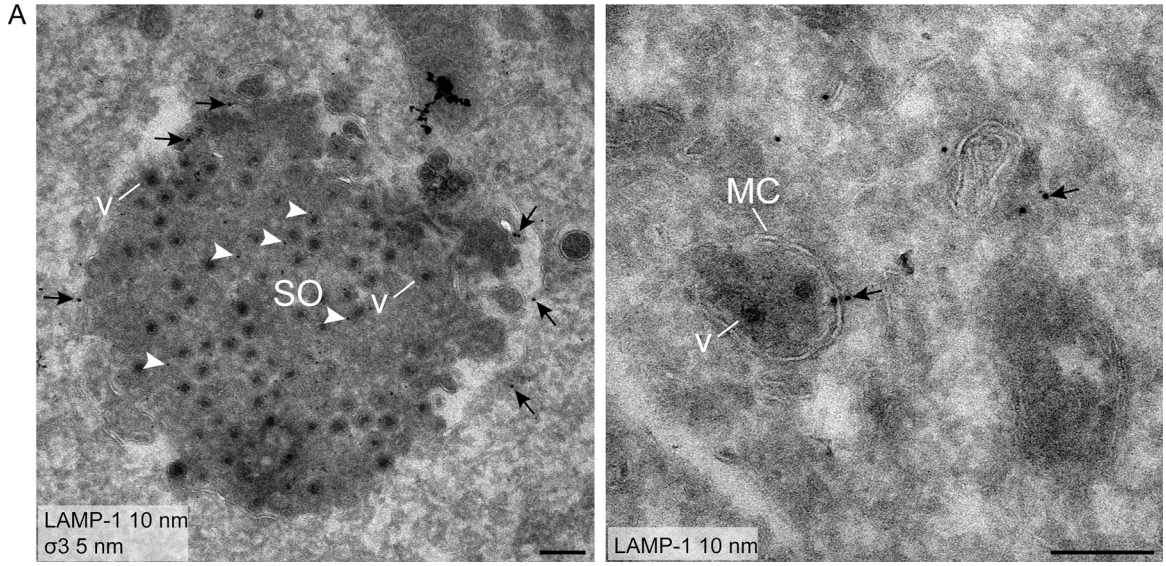

Figure 6. **Immunogold labeling of LAMP-1 and σ3 in reovirus-infected HBMECs.** HBMECs were adsorbed with reovirus T1L M1-P208S at an MOI of 1 PFU/cell and cryosectioned using the Tokuyasu method at 18 hpi. Sections were immunogold labeled for LAMP-1 or σ3 (rabbit VU219) using secondary antibodies conjugated with 10- or 5-nm gold particles, respectively. **(A)** A high-magnification view of a virion-filled SO labeled for LAMP-1 (arrows) and σ3 (arrowheads) is shown on the left. V, virion. An MC filled with virions is shown in the right panel and also labeled for LAMP-1 (arrows). Scale bars, 200 nm.

were observed by TEM to surround inclusions (Fig. S4, E and F). Redistribution of lysosomes was observed in 90% and 92.3% of cells infected with T1L and T3D, respectively (Fig. S4G). Therefore, lysosome recruitment to VIs occurs in the majority of reovirus-infected cells, independently of the host cell type or viral strain. Collectively, our results show that the reovirus egress machinery is a superstructure assembled on the periphery of VIs. This structure is composed of SOs formed from modified lysosomes that collect mature virions from VIs and MCs that bud from SOs and transport virions to the plasma membrane.

Defects in lysosome dynamics alter reovirus infection

To confirm a requirement for lysosome recruitment to VIs in reovirus egress, we blocked the movement and function of lysosomes using the lysosomotropic weak base ammonium chloride (NH_4Cl; Ohkuma and Poole, 1978; Seguin et al., 2014). To avoid inhibition of reovirus entry (Dermody et al., 1993; Sturzenbecker et al., 1987), HBMECs were infected with reovirus for 24 h, at which time >90% of cells are infected, incubated for an additional 24 h with or without 20 mM NH_4Cl, and imaged using confocal microscopy and EM (Fig. 7). Confocal microscopy showed that in untreated cells, lysosomes accumulate around VIs and incorporate virions (Fig. 7 A, left). However, in NH_4Cl^--treated cells, lysosomes surrounding inclusions do not contain virions (Fig. 7 A, right). Treatment of cells with NH_4Cl reduced infectious intracellular and extracellular viral particles by 100-fold (Fig. 7 B). EM revealed additional details (Fig. 7, C and D). At 48 hpi, in untreated cells, SOs around VIs contained mature virions (Fig. 7 C, image on the left). However, in NH_4Cl^--treated cells, lysosomes and SO-like structures near VIs did not (Fig. 7 C, image on the right). Characteristic MCs observed in untreated cells were not detected in cells treated with NH_4Cl (Fig. 7 D). Together, these data indicate that lysosomes are key elements of the reovirus egress machinery.

Endosomes are not recruited to VIs

To investigate whether other organelles within the endocytic pathway are recruited to reovirus inclusions, we determined the distribution of late and recycling endosomes in HBMECs by immunofluorescence and confocal microscopy (Fig. S5). Following internalization into cells, primary endocytic vesicles undergo multiple rounds of homotypic fusion to form early, late, and sorting endosomes (Salzman and Maxfield, 1988). Both in uninfected and reovirus-infected HBMECs, Rab11-positive recycling endosomes have a diffuse distribution in the cytosol (Fig. S5, A and B, left panels). The mannose-6-phosphate receptor (M6PR), which is a specific marker of late endosomes and not present in mature lysosomes (Kirkbride et al., 2012), accumulates near the nucleus in both uninfected and reovirus-infected cells (Fig. S5, A and B, right panels). Unlike lysosomes, neither Rab11- nor M6PR-positive endosomes redistributed to VIs in reovirus-infected cells. We conclude that, unlike lysosomes, endosomes are not recruited to VIs.

Total internal reflection fluorescence (TIRF) microscopy reveals that the reovirus egress machinery moves to specific areas at the base of cells

To image reovirus egress in real time during infection, we used superresolution live-cell microscopy. HeLa cells were first transfected with a σ3-GFP plasmid for 24 h and then adsorbed with reovirus for 1 h. At 16 hpi, cells were incubated with LysoTracker and imaged using TIRF microscopy to analyze basal reovirus egress zones (Fig. 8). Lysosomes and reovirus σ3-GFP capsid protein signals colocalized in infected cells, moving to specific areas at the base of the cell (Videos 7 and 8; arrows in

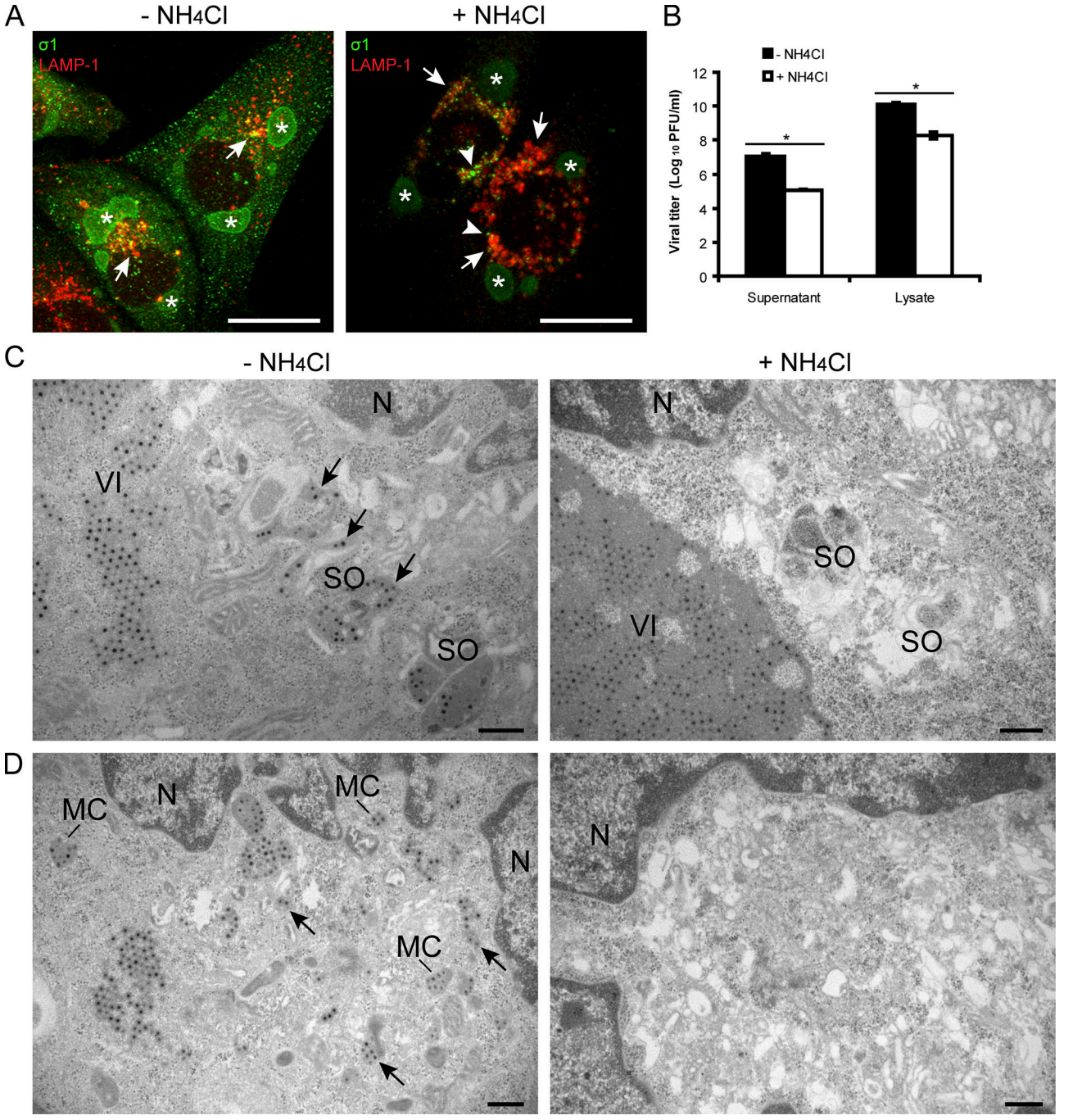

Figure 7. **Effect of ammonium chloride on the reovirus egress machinery.** HBMECs were either mock infected or adsorbed with reovirus strains T3D and T1L M1-P208S at an MOI of 1 PFU/cell, treated at 24 hpi with 20 mM ammonium chloride (NH_4Cl), and incubated for an additional 24 h. Cells were fixed and processed for confocal microscopy and EM. **(A)** Confocal microscopy of infected cells incubated in the absence or presence of NH_4Cl and stained with mouse anti-σ1 monoclonal antibody 9GB5 (green). Lysosomes are labeled with anti-LAMP-1 (red). In untreated T3D-infected cells (image on the left), lysosomes with virions (arrows) surround VIs (asterisks). In the perinuclear region of infected cells treated with NH_4Cl (image on the right), lysosomes near VIs do not contain virions (arrows), and reovirus σ1 protein concentrates in perinuclear puncta (arrowheads). Scale bars, 25 µm. **(B)** HBMECs were adsorbed with reovirus T1L-M1-P208S at an MOI of 1 PFU/cell and either untreated or treated with NH_4Cl. Titers of extracellular (supernatant) and intracellular (cell lysate) virus were determined by plaque assay. The results are presented as mean ± SEM of three independent experiments, each with two technical replicates. *, $P < 0.05$, unpaired two-tailed Student's *t* test. **(C and D)** EM of T1L-M1-P208S-infected cells incubated with or without NH_4Cl. **(C)** In untreated infected cells, modified lysosomes (SOs) near VIs contain mature virions (arrows). In NH_4Cl-treated cells, SO-like structures without virions are observed near VIs. **(D)** MCs with mature virions are observed in the cytoplasm of untreated infected cells. MCs filled with virions are not detected in cells treated with NH_4Cl. N, nucleus. Scale bars, 500 nm.

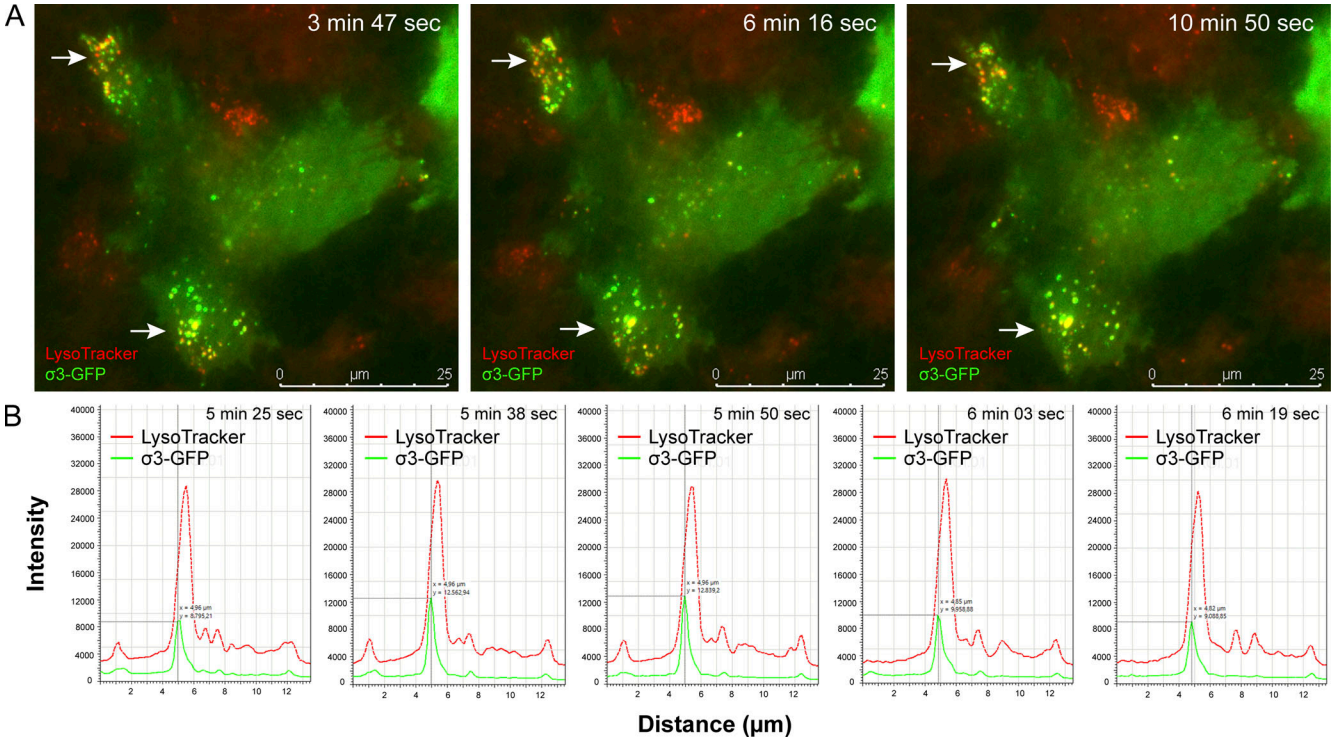

Figure 8. **Superresolution live cell microscopy of lysosomes in reovirus-infected cells.** HeLa cells were transfected with a σ3-GFP plasmid for 24 h and adsorbed with reovirus T1L M1-P208S at an MOI of 10 PFUs/cell. At 16 hpi, cells were imaged using TIRF microscopy to visualize basal reovirus egress zones. **(A)** TIRF microscopy images showing lysosomes stained with LysoTracker (red) and σ3 visualized with the GFP fusion protein (green). Arrows indicate the association of lysosomes and reovirus σ3 over time. **(B)** Fluorescence signal intensity corresponding to lysosomes and reovirus was quantified in a representative area using LAS X software (Leica Microsystems). The graphs confirm the colocalization of signals associated with LysoTracker and σ3-GFP. Another example of a reovirus-infected cell is shown Videos 7 and 8. A time-lapse recording of uninfected cells is shown in Video 9.

Fig. 8 A). We confirmed the colocalization of both signals by quantifying the distribution of mean fluorescence intensity over time in a single region of interest (Fig. 8 B). In contrast to the random movement of lysosomes at the base of uninfected cells (Video 9), lysosomes associated with reovirus σ3-GFP (yellow) in transfected-infected cells moved rapidly throughout the cell and distributed in highly dynamic pools at the cell periphery (Videos 7 and 8).

To confirm that reovirus σ3-GFP protein encapsidates on to infectious virions during infection, we analyzed its distribution by immunofluorescence (Fig. S5, C–F). Confocal microscopy of transfected-infected cells showed that σ3-GFP incorporates into reovirus inclusions during infection (Fig. S5, C–E). In addition, σ3-GFP showed the same distribution pattern in some inclusions as its capsid-binding partner, μ1 (arrows in Fig. S5 E, right panels). Supernatants from transfected and infected cell cultures were collected at 24 and 48 hpi and used to infect fresh HeLa cell monolayers. A small percentage of cells was infected by the σ3-GFP virus, 2% and 4% when cells were adsorbed with supernatants collected at 24 and 48 hpi, respectively (Fig. S5 F). These cells demonstrated intracellular GFP signals (Fig. S5 F, left), whereas supernatants of transfected-uninfected cells displayed no detectable fluorescence. These results confirm that a small percentage of virions released from transfected/infected cells are encapsidated by the σ3-GFP protein and can be used to study virus egress by live-cell microscopy (Fig. 8 and Videos 7 and 8). Taken together, superresolution TIRF microscopy demonstrates that the reovirus egress machinery moves to specific areas at the base of cells before exit of viral progeny.

VI–SO–MC interfaces are physically connected through discrete membrane fusion points

Examination of the VI–SO–MC interfaces by ET revealed that there are physical connections between these structures (Fig. 9). The computational slices of the tomogram, together with the 3D model, shows that there are points of membrane fusion connecting VIs and SOs (dashed boxes in Fig. 9 A). Analysis of MCs by 2D TEM suggests that these structures emerge from SOs (Fig. 3 C), as the MC membranes are fused with SO membranes. By 3D ET, the MC membrane connects with that of the SO to form a membranous channel (Fig. 9 B, dashed boxes). The tomogram shown in Fig. 9 B was obtained from a semithick section (~400 nm), which facilitates detection of interactions and connections between large, complex structures. Using this approach, the connections between both VI–SO and SO–MC are restricted to a few computational slices. Therefore, interactions between these structures may occur through discrete membrane fusion points or channels like those shown in Fig. 9. We analyzed nine tomograms and observed in each physical VI–SO–MC interconnections via discrete points of membrane fusion.

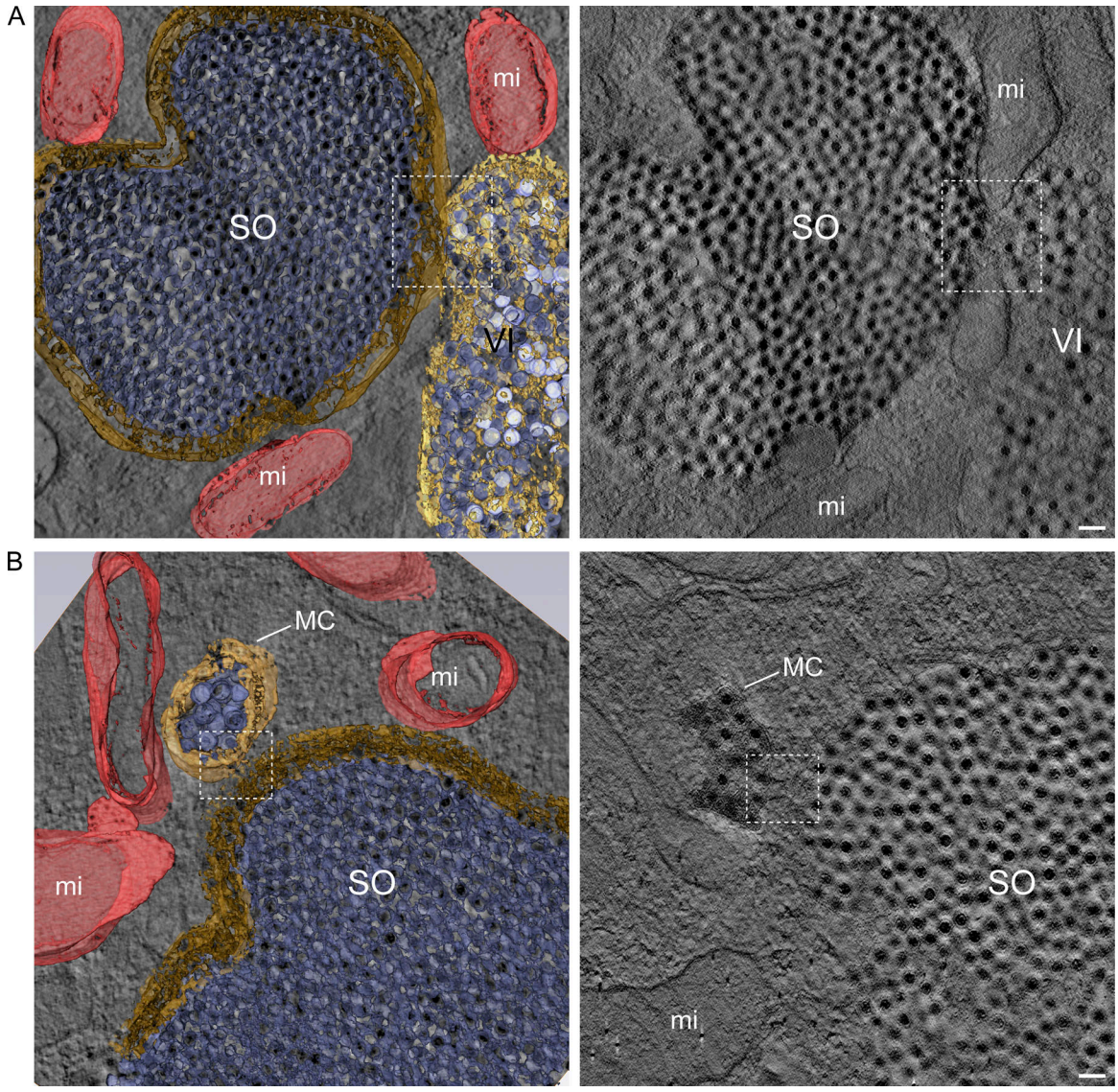

Figure 9. **ET of reovirus egress machinery.** HBMECs were adsorbed with reovirus T1L M1-P208S at an MOI of 1 PFU/cell and processed at 18 hpi by high-pressure freezing, freeze substitution, semithick sectioning, and TEM. **(A and B)** Single-tilt tomography. 3D reconstruction and computational tomography slices show details of the connection between the components of the reovirus egress machinery. The dashed box marks the specific point of membrane connection between an SO and a VI (A) and an MC linked to an SO through a channel (B). mi, mitochondrion. Scale bars, 200 nm.

Discussion

Viral egress and cell-to-cell transmission serve as important potential targets for antiviral therapeutics. In this study, we imaged the egress machinery used by reovirus to exit HBMECs in a nonlytic manner. Previous studies using polarized HBMECs showed that reovirus exits cells predominantly via the apical surface (Lai et al., 2013). Here, we used nonpolarized HBMECs and found that progeny virions exit cells at discrete zones at the basal surface. A detailed ultrastructural study showed that the reovirus egress machinery is composed of two different virus-induced, membranous elements, SOs and MCs, which are shown schematically in Fig. 10. SOs are modified lysosomes recruited to VIs. These organelles coalesce around the VI periphery and appear to selectively collect mature virions. Through a mechanism that remains unclear, smaller MCs bud from SOs, move to the cell periphery, fuse with the plasma membrane, and release virions to the extracellular space.

In reovirus-infected cells, mature virions are attached to filaments, whereas empty particles are not. These filamentous attachments are observed inside VIs and maintained in SOs, MCs, and the extracellular environment. The identity of the filaments is not apparent from our study, but they may be formed from actin based on their morphology. Therefore, it is possible that actin-like filaments are involved in the mechanism that mediates reovirus sorting at the VI periphery before egress, in which only mature virions are collected for sorting into the egress machinery.

The morphology of SOs recruited to the VI periphery is compatible with lysosomes or autolysosomes. Autophagosomes normally fuse with lysosomes to form autophagolysosomes or

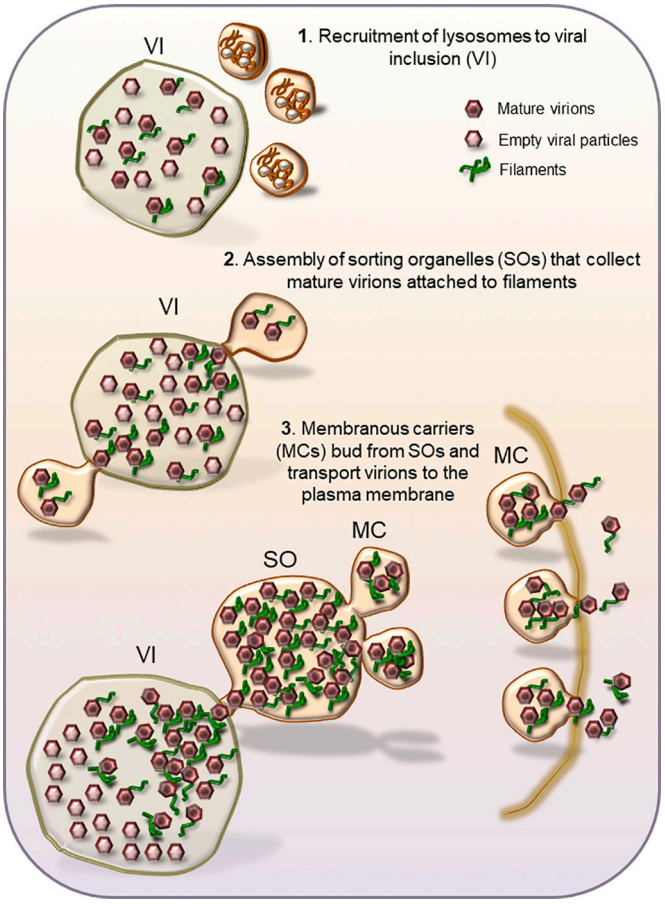

Figure 10. **Model of the reovirus egress machinery.** VIs contain membranes and filaments that are bound to mature virions. Lysosomes are recruited to VIs and become SOs, which collect mature virions likely by a filament-dependent mechanism. When virions become densely packed inside SOs, smaller MCs bud from the SOs. MCs move to the cell periphery, fuse with the plasma membrane, and release virions into the extracellular medium.

autolysosomes (Klionsky et al., 2014). Autophagy is a highly conserved recycling pathway characterized by the formation of double-membraned vesicles and subsequent degradation and recycling of cytosolic contents. The autophagy machinery also contributes to unconventional secretion, which is used by some viruses to exit infected cells (Mutsafi and Altan-Bonnet, 2018). Of note, autophagic processes may facilitate infection by some reoviruses (Chen et al., 2017; Kemp et al., 2017). However, markers for autophagosomes (LC3 and monodansylcadaverine) do not label SOs, and drugs that induce or block autophagy do not alter reovirus infection in HBMECs (data not shown). Based on (1) labeling of SOs with LysoTracker and LAMP-1; (2) the observed changes in lysosome number, size, and distribution during reovirus infection of HBMECs; (3) the identification of SOs and MCs marked with LAMP-1 in thawed cryosections; and (4) the effects of NH_4Cl on reovirus egress, we conclude that SOs are not autophagolysosomes but modified lysosomes. SOs were labeled with anti-LAMP-1 antibodies, but immunofluorescence with anti-cathepsin antibodies did not label these organelles (data not shown). Lysosomes recruited to the VI periphery exhibit a variety of pH values as shown by the color of the fluorescent probes (Fig. S3). However, the largest organelles with or without virions contained within have a pH ∼6.1, suggesting that the pH of lysosomes is modified following recruitment to VIs and before incorporation of virions. Moreover, if hydrolytic enzymes are contained within SOs, at a pH of ∼6.1, these enzymes should not be active, and progeny viral particles should not be degraded. In addition, the filaments attached to the progeny particles within the lysosome-derived SOs may contribute to protection of mature virions from premature disassembly.

The participation of lysosomes in reovirus egress was an unexpected finding, as was the discovery that reovirus infection induces an increase in the number and size of lysosomes. NH_4Cl blocks the production of infectious progeny in reovirus-infected cells by preventing the proteolytic processing of viral outercapsid proteins by acid-dependent cellular proteases in late endosomes or lysosomes during viral entry (Ebert et al., 2002; Sturzenbecker et al., 1987). However, infection with ISVPs, which can penetrate cell membranes and do not require endosomal proteases for disassembly, is not affected by NH_4Cl treatment (Dermody et al., 1993; Sturzenbecker et al., 1987). We tested the effect of incubating cells with NH_4Cl at 24 hpi, when >90% of cells in the monolayer are infected. Our results show that lysosomes have a second role in reovirus infection; a subset of these organelles participates in reovirus egress, as lysosome-derived SOs selectively collect mature virions from VIs. Treatment with NH_4Cl interferes with lysosome transport and function during reovirus infection, which impairs collection of mature virions from VIs and diminishes virus egress. Additionally, treatment of cells with NH_4Cl neutralizes the pH of lysosomes and blocks incorporation of mature virions from VIs into SOs. How these lysosomes/SOs are recruited to VIs and how they package mature virions is not clear from our experiments, although our results suggest that the filaments bound to mature virions might have a function in this process (Fig. 10).

Some viruses use modified lysosomes as replication organelles. For example, members of the Togaviridae family, such as rubella virus and Semliki Forest virus, replicate their genomes in specialized structures assembled at the plasma membrane. These structures become internalized, producing vesicles that eventually fuse with lysosomes to form cytopathic vacuoles. These virus-induced organelles become enwrapped by rough ER and function as sites of viral RNA synthesis (Fontana et al., 2007, 2010; Frolova et al., 2010; Lee et al., 1994; Magliano et al., 1998; Spuul et al., 2010). Although reovirus does not appear to incorporate lysosomal machinery within VIs, our data demonstrate a function for lysosomes in the transport and release of progeny particles from infected cells.

The endosomal–lysosomal system is composed of intracellular membranous compartments that dynamically interconvert and consists of early endosomes, recycling endosomes, late endosomes, and lysosomes. The pH of the endocytic compartment progressively decreases from early endosomes (pH 6.8–6.0) to late endosomes (pH 6.0–5.0) and lysosomes (pH <5.0). Lysosomes are single-membrane–bound organelles that have an acidic lumen and contain several types of hydrolases involved in

the degradation of biomolecules. Thus, the main function of lysosomes in cells and also during some viral infections is proteolysis. However, we observed that mature reovirus virions are collected from inclusions and placed inside modified lysosomes for eventual transport to the plasma membrane. Alterations of endosomal pH, either increased or decreased, inhibit reovirus infection by preventing capsid disassembly (Thete and Danthi, 2015). Therefore, late endosomes, and not lysosomes, have the optimal pH and host factors required to uncoat reovirus during cell entry. However, endosomes are not recruited to mature VIs, suggesting that these endocytic organelles do not function in late steps in reovirus infection.

Lysosomes also participate in other cellular processes such as plasma membrane repair, cell signaling, and energy metabolism (Settembre et al., 2013). Lysosomal contents can be released following fusion with the plasma membrane, which occurs constitutively in some cell types such as immune cells (Griffiths, 2016), but any cell can perform this function (Rodríguez et al., 1997; Settembre et al., 2013). Lysosomal exocytosis functions to repair cell membranes, a process important in defense against bacterial infections (Roy et al., 2004). The SOs identified in this study are modified lysosomes that appear to collect mature virions from the periphery of VIs. ET of the VI–SO interface confirms that there are points of membrane fusion connecting these structures. Considering that VIs are formed from membranes (Fernández de Castro et al., 2014) and that viral particles inside VIs are attached to membranes (Tenorio et al., 2018), mature virions may be transferred to SOs by these membrane connections with the assistance of filaments. These specific points of membrane connection or membrane-contact sites have been described for different organelles. For example, StAR-related lipid transfer domain-3 is a sterol-binding protein that mediates ER–endosome contact sites (Wilhelm et al., 2017). In the case of reovirus infection, VIs are formed by a network of ER membranes (Tenorio et al., 2018). Interaction of the VI-associated ER network with lysosome-derived SOs could be mediated by similar contacts. These types of membrane-contact sites require lipid and cholesterol transport (Wilhelm et al., 2017). Interestingly, SO contents stain with the cholesterol marker filipin (data not shown). Thus, reovirus may use both viral and cellular proteins to establish these contacts and transport mature virions efficiently through the egress machinery.

In a second step of the reovirus egress process, small MCs bud from SOs and transport progeny virions to the plasma membrane. Like SOs, MCs also contain lysosome markers LysoTracker and LAMP-1. It is not apparent how the SO fragmentation takes place, but we speculate that the close apposition of viral particles inside the SOs could provoke the budding of the smaller MCs containing fewer virions. Lysosomal membrane glycoproteins cycle from lysosomes to endosomal compartments and the cell surface. Clathrin coats and vesicles form on lysosomes, and it is possible that these vesicular elements are responsible for protein and membrane trafficking out of this compartment (Traub et al., 1996). In the case of reovirus, the budding mechanism that produces the MCs might differ, as we have not observed the formation of coats on SO membranes. ET of the SO–MC interface shows that both structures are connected by a membranous channel that is consistent with a budding mechanism. A related pathway has been described for hepatitis C virus egress, in which multivesicular bodies mediate viral particle release. Blocking multivesicular body activity leads to an accumulation of viral particles in exosomes, illustrating the importance of the endosomal pathway for hepatitis C virus replication (Elgner et al., 2016).

Monitoring individual viruses by labeling viral structural components with fluorescent proteins is a powerful strategy for studies of viral assembly and egress. With this approach, the location and kinetics of assembly as well as the exit mechanisms of progeny virions can be ascertained. We investigated interactions of reovirus particles with lysosomes in living cells by expressing reovirus σ3-GFP capsid protein during reovirus infection. The σ3-GFP capsid protein incorporates into newly formed virions, which allowed us to track progeny virions in real time using TIRF microscopy. Although TIRF microscopy is a wide-field imaging technique that allows signal preservation for extended observation intervals, the excitation depth of an evanescent wave generated by total internal reflection is only 100–200 nm (Brandenburg and Zhuang, 2007), limiting its application to events that take place near the cell surface. Importantly, after the initial steps of assembly, the TIRF signal becomes sufficiently strong to track viral egress at the single-virion level. Using TIRF superresolution light microscopy, we observed single reovirus particles exiting cells, thus obtaining dynamic information about the egress mechanism. These studies strengthen the conclusion that most mature virions are associated with lysosomes and move to discrete locations at the cell periphery before egress. Analogous to our studies with reovirus, a similar strategy has been applied to analyze HIV-1 Gag in cells. Gag molecules are initially diffuse in the cytosol and later accumulate in perinuclear clusters. They are then transported through multivesicular bodies before distribution to the plasma membrane (Perlman and Resh, 2006). TIRF studies also have demonstrated that the assembly of bluetongue virus, a member of the Reoviridae family, depends on the distinct cellular distribution of core proteins VP3 and VP7 (Kar et al., 2005).

We have identified two key elements of the machinery mediating nonlytic reovirus egress: SOs, which are modified lysosomes and MCs, which bud from SOs. Filaments connect virions within the VI–SO–MC superstructure to the plasma membrane. Important questions remain: Does reovirus recruit and transform lysosomes into SOs by interacting with lysosomal membrane proteins or lipids? How are mature virions recognized by SOs? How do MCs with virions bud from SOs? Our ongoing work to answer these questions will clarify the functional elements of the reovirus egress pathway and may illuminate new targets for antiviral intervention.

Materials and methods

Cells and viruses

HBMECs were grown in RPMI medium 1640 supplemented to contain 10% FBS (BI Biological Industries), 10% Nu Serum (Corning), 1% MEM-vitamins (Gibco), 1% sodium pyruvate

(Gibco), 1% MEM nonessential amino acids (Sigma-Aldrich), 1% L-glutamine (Merck), 1% penicillin/streptomycin (Sigma-Aldrich), and 0.1% amphotericin B (Sigma-Aldrich). HeLa CCL2 and Vero cells were grown in DMEM (Sigma-Aldrich; D6429) supplemented to contain 10% FBS, 1% sodium pyruvate (Gibco), 1% MEM nonessential amino acids (Sigma-Aldrich), 1% L-glutamine (Merck), 1% penicillin/streptomycin (Sigma-Aldrich), and 0.1% amphotericin B (Sigma-Aldrich).

Cells were infected with reovirus strain T1L M1-P208S, which is identical to the prototype T1L strain except for a proline-to-serine substitution at position 208 of the μ2 protein (M1 gene). This mutation changes inclusion morphology from filamentous to globular (Parker et al., 2002), which allows inclusions to be more apparent for imaging experiments. For some experiments, cells were infected with reovirus strains T1L or T3D. These viruses were recovered by plasmid-based reverse genetics (Kobayashi et al., 2007). All reovirus strains were purified by cesium gradient centrifugation as described previously (Furlong et al., 1988) and propagated at an MOI of 5 PFUs/cell at 33°C for 65 h to generate working stocks. Viral titers were determined by plaque assay using spinner-adapted murine L929 fibroblast cells (Virgin et al., 1991). ISVPs were prepared by treatment of virions with chymotrypsin (Sigma-Aldrich; Baer and Dermody, 1997).

A plasmid encoding a T3D σ3-GFP fusion protein was engineered by synthesizing linear fragments of the pcDNA3.1+-GFP vector and T3D σ3-encoding S4 gene cDNA by PCR amplification using the following primers: pcDNA3.1-GFP An T3D S4 SEG1 FP, 5′-TTAAACTTAAGCTTGGTACCATGGAGGTGTGCT TGCCC-3′

pcDNA3.1-GFP An T3D S4 SEG3 RP; 5′-TCCTCGCCCTTGCTC ACCATACCAGAACCACCACCAGAACCACCGCCAAGAATCATC GGATC-3′; T3D S4 An pcDNA3.1-GFP FP, 5′-GGTGGTTCTGGT GGTGGTTCTGGTATGGTGAGCAAGGGCGAG-3′; T3D S4 An pcDNA3.1-GFP RP, 5′-CATGGTACCAAGCTTAAGTTTAAACG-3′. Fragments were assembled by Gibson Assembly (NEB; E2611) according to the manufacturer's instructions.

Infections and ammonium chloride treatment

Cells were adsorbed with reovirus at MOIs of 1, 5, 10, or 20 PFUs/cell (stocks diluted in culture medium) at 37°C for 1 h. After the inoculum was removed, fresh medium supplemented to contain 2% FBS was added, and cells were incubated for various intervals. Maximum virus release is in the exponential phase of replication, which corresponds to 18–24 hpi.

HBMECs were either mock infected or adsorbed with reovirus at an MOI of 1 PFU/cell, treated at 24 hpi with 20 mM ammonium chloride (Sigma-Aldrich; 09718, NH_4Cl), and incubated for an additional 24 h. Cells were fixed and processed for confocal microscopy and EM. Supernatants were collected and cell lysates prepared from all experimental conditions for virus titration by plaque assay.

Immunofluorescence, confocal, and STED microscopy

Cells were grown on glass coverslips, fixed with 4% PFA (TAAB Laboratories), and washed three times with cytoskeleton buffer, pH 6.1 (150 mM NaCl, 10 mM MES, 5 mM MgCl, 5 mM EGTA, and 5 mM glucose). Cells were incubated with 50 nM LysoTracker Red DND-99 (Invitrogen; L7528) at 37°C for 30 min before fixation. Fixed cells were permeabilized by incubation for 40 min with cytoskeleton buffer containing 0.25% saponin and 2% FBS. Cells were incubated for 1 h with primary antibodies diluted 1/200 in cytoskeleton buffer with saponin and FBS. The following antibodies were used: rabbit anti-reovirus polyclonal antiserum, mouse 10C1 anti-σ3 monoclonal antibody (conformation-specific antibody, used to label native σ3; Virgin et al., 1991), rabbit VU219 anti-σ3 polyclonal antiserum, mouse 8H1 anti-σ3 monoclonal antibody, mouse 5C6 anti-σ1 monoclonal antibody specific for T1L σ1, mouse 9GB5 anti-σ1 monoclonal antibody specific for T3D σ1, mouse 8H6 anti-μ1 monoclonal antibody, rabbit anti-LAMP-1 polyclonal antiserum (Abcam; ab24170), rabbit anti-M6PR (M6PR, cation dependent) monoclonal antibody (Abcam; ab134153), and rabbit anti-Rab11A polyclonal antiserum (Invitrogen; 71–5300). Alexa Fluor–conjugated antibodies (Invitrogen) were used as secondary antibodies. Cell nuclei and actin were stained with DAPI (Sigma-Aldrich) and phalloidin (Sigma-Aldrich; Phalloidin-TRITC, P1951; or Life Technologies; Phalloidin Alexa Fluor 488, A12379), respectively, diluted 1/200 in cytoskeleton buffer (0.25% saponin and 2% FBS) for 20 min. The plasma membrane was labeled with the lectin WGA WGA-647 (Life Technologies). All incubations were conducted at RT. Some cells were processed for immunofluorescence without saponin permeabilization. Coverslips were mounted using Prolong-Gold (Life Technologies). Confocal micrographs were acquired using a Leica TCS SP5 confocal multispectral microscope equipped with an HCX PL APO 63.0 X/1.4 NA oil objective and LAS AF v.2.7.3 software (Leica Microsystems). STED analysis was conducted using a Leica TCS SP8 STED microscope equipped with an HC PL APO CS2 100×/1.4 NA oil objective and LAS X software (Leica Microsystems).

Mean fluorescence intensity of immunofluorescence images was quantified by selecting 50 regions of interest with a size of 9 μm^2. These regions were selected randomly at <5 μm or >15 μm from the nuclear rim in uninfected and reovirus-infected cells using LAS X software (Leica Microsystems). The mean fluorescence intensities of control and infected cells were compared using an unpaired, two-tailed Student's *t* test.

Lysosome number and size were quantified by acquiring images using a Leica TCS SP5 confocal multispectral microscope with an objective of 63× and an enlargement factor of 3. The diameter of lysosomes varies from 0.1 to 1 μm (Xu and Ren, 2015). Therefore, individual lysosomes were defined as having a size of 0.0078 to 0.78 μm^2 and aggregated lysosomes as having a size ≥0.78 μm^2 (calculated from πr^2). The size by area in μm^2 of lysosomes per cell was determined using ImageJ-Fiji software. Images were first converted to binary images by thresholding, in which the foreground pixel value was assigned 250, and background pixel values were assigned the minimum possible value (0). Binary images were segmented using the watershed algorithm that separates different objects (lysosomes) of the image, allowing masked or segmented images to be obtained. Finally, lysosome number and area of each segmentation were placed into arrays from which the lysosomal network morphology was

calculated. The mean number and size of lysosomes in uninfected and reovirus-infected cells was compared with Prism8 software using an unpaired, two-tailed Student's *t* test. A total of 52 cells and ∼3,000 lysosomes per group were analyzed.

Live-cell imaging

HBMECs were cultivated on glass-bottom culture p35 plates (Ibidi) and adsorbed with reovirus at an MOI of 1 PFU/cell for 1 h. Cells were labeled with 50 nM LysoTracker Red DND-99 (Invitrogen; L7528) to visualize lysosomes. From 1 to 24 h postadsorption, fluorescence and phase-contrast images were collected every 30 min using a Leica DMI6000B fluorescence microscope equipped with an HC PL FLUO 40×/0.75 objective and LAS X software. Infected cells were identified by the presence of VIs, which appear by phase-contrast microscopy as dense, globular structures. High-resolution movies were made using a Leica DMI6000B fluorescence microscope equipped with an HCX PL APO 63×/1.30 Gly objective. Fluorescence and phase-contrast images were collected every 30 min from 20 to 23 h post infection.

Single-particle tracking was conducted using the TrackMate (Tinevez et al., 2017) plugin of ImageJ-Fiji. This approach allows segment spots or roughly spherical objects to be collected from an image and tracked over time. Individual lysosomes (∼0.5–1 µm in diameter) were followed in selected frames of the live-cell imaging movies using a Differences of Gaussian (DOG) detector and generic segmentation algorithms. Each spot was assigned a series of numerical features calculated using its location, radius, and mean pixel intensity. A threshold was manually established, and spots with a quality value below this threshold were discarded. The threshold value was 0.58, and the total intensity filter on spots selected was 1.89. The HyperStack displayer was used for spot visualization, and the Linear Assignment Problem (LAP) tracker was used for the particle-linking algorithm.

Measurement of pH of endosomes and lysosomes

HBMECs were adsorbed with reovirus T3D at an MOI of 1 PFU/cell for 1 h. At 4 hpi, cells were incubated with a 10,000-D dextran coupled to FITC and a 70,000-D dextran coupled to rhodamine (Sigma-Aldrich; fluorescein isothiocyanate–dextran and rhodamine B isothiocyanate–dextran) at 1 mg/ml for 16 h in medium without serum (Meo-Evoli et al., 2015). The medium was removed, and cells were fixed with 4% PFA before imaging.

Fluorescence signal calibration was determined by incubating cells with an isotonic potassium buffer (130 mM KCl, 1 mM $MgCl_2$, 15 mM Hepes, and 15 mM MES, containing 10 µM nigericin and 10 µM valinomycin; Sigma-Aldrich). The pH of the buffer was adjusted to 4.5, 5.0, 5.5, 6.0, 6.5, or 7.0 (Christensen et al., 2002).

Fluorescence images were obtained using a Leica DMi8 S wide-field epifluorescence microscope equipped with a phase-contrast 63× oil-immersion objective. For each experimental and calibration-curve condition, images from 20 different regions of cell monolayers were acquired (a total of >600 cells per condition) using excitation wavelengths of 488 for FITC and 568 for rhodamine. Simultaneously, phase-contrast images were acquired from the same regions. Images of the peri-VI (pVI) organelles were acquired using a confocal multispectral Leica TCS SP5 microscope equipped with a phase-contrast 100× oil-immersion objective, pinhole set at 1 Airy unit, and LAS AF software. Images are enlarged twice from a single confocal image using the same parameters described.

Fluorescence signals were processed using ImageJ-Fiji software. A binary image was produced using an adjusted threshold of the rhodamine images in order to include only labeled organelles in the calculations. The binary mask was overlaid on the FITC image, and rhodamine background was subtracted. Signal intensity was computed from all 20 images for each condition. Measurements were exported to Microsoft Excel, and a ratio of FITC and rhodamine signal from the segmented images was calculated. Image acquisition and processing of the calibration curves were conducted using the same strategy. The pH of labeled organelles was determined from the green-to-red ratio by comparison to standard curves established for each experiment.

The pVI signal was quantified by collecting 103 selection masks from single labeled organelles adjacent to VIs in order to obtain the FITC and rhodamine data. The green-to-red ratio was extrapolated to pH values as described. The data were analyzed with Microsoft Excel. FITC/rhodamine ratios were extrapolated to pH using the polynomial adjusted regression line from the calibration curve. Results are presented as the average pH of labeled organelles for each condition (uninfected cells, infected cells, and pVI) of three independent experiments. Experimental datasets were compared using a two-sample, two-tailed, and unequal SD Student's *t* test. Values of *, $P < 0.05$; **, $P < 0.01$; and ***, $P < 0.001$ were considered statistically significant. In cell monolayers incubated with FITC–dextran and rhodamine B–dextran, a total of 16 zones with 55 pVI lysosome-like organelles were mapped by confocal microscopy. Selected cells and lysosome-like organelles were visualized again by confocal microscopy after immunofluorescence with a mouse monoclonal antibody 9GB5 specific for T3D σ1 protein.

TIRF microscopy

HeLa cells were transfected with a σ3-GFP plasmid using FuGENE 6 (Promega; E269A) transfection reagent. At 24 h post-transfection, cells were adsorbed with reovirus T1L M1-P208S at an MOI of 10 PFUs/cell for 1 h. At 16 hpi, cells were labeled with 50 nM LysoTracker Red DND-99 to visualize lysosomes. TIRF images were collected every 3 s thereafter for 30 min using a Leica DMi8 S widefield epifluorescence microscope equipped with a Hamamatsu Flash 4 sCMOS digital camera and an HC PL APO 100×/1.47 oil objective. The TIRF module was equipped with a Hamamatsu W-View Gemini for simultaneous GFP/mCherry TIRF image acquisition. Images and movies were processed using LAS X software.

TEM

Infected HBMECs were grown on sapphire discs (Leica microsystems) and processed by high-pressure freezing. Sapphire discs were carbon-coated and incubated at 130°C for 8 h to stabilize the carbon. After sterilization (1 h under UV light), the discs were incubated with RPMI before adding HBMECs. Cells were adsorbed with reovirus, incubated for 18 h, fixed with 1%

glutaraldehyde in 0.4 M Hepes buffer, pH 7.2, at RT for 1 h, and frozen with an Empact instrument (Leica Microsystems). Frozen cells were processed by freeze substitution in a mixture of 1% osmium tetroxide, 0.1% uranyl acetate, 5% water, 2% methanol in dry acetone using an AFS instrument (Leica Microsystems). After substitution, samples were gradually infiltrated with epoxy resin. Polymerization was conducted in flat-bottom beam capsules at 60°C for 48 h.

For conventional EM, cells were grown on sterile Thermanox Plastic Coverslips (Nunc) before infection and drug treatment. Cells were adsorbed with reovirus, incubated for 18 h, and fixed with a mixture of 4% PFA and 1% glutaraldehyde in 0.4 M Hepes buffer, pH 7.4, at RT for 1 h. Cells were postfixed by incubation at 4°C for 1 h with a mixture of 1% osmium tetroxide and 0.8% potassium ferricyanide in water and dehydrated in 5-min steps with increasing concentrations of acetone (50%, 70%, 90%, and twice in 100%) at 4°C. Samples were processed for flat embedding in the epoxy resin EML-812 (TAAB Laboratories) by incubating overnight with a 1:1 mixture of acetone-resin at RT. Cells were infiltrated for 8 h in pure resin and polymerized at 60°C for 48 h. Ultrathin (~50–70 nm) oriented serial sections were obtained using an UC6 ultramicrotome (Leica Microsystems), collected on uncoated 300-mesh copper grids (TAAB Laboratories), stained with saturated uranyl acetate and lead citrate, and imaged by TEM. Images were acquired using a JEOL JEM 1011 electron microscope operating at 100 kV equipped with a Gatan ES1000Ww digital camera.

For immunolabeling thawed cryosections, cells were fixed at 18 hpi with 4% PFA in PHEM buffer, pH 7.2 (60 mM Pipes, 25 mM Hepes, 10 mM EGTA, and 2 mM $MgCl_2$) at RT for 2 h. Fixed monolayers were incubated with 50 mM NH_4Cl to quench free aldehydes groups. Cells were removed from the plastic plate using a rubber policeman and pelleted in a 1.5-ml Eppendorf tube. Pellets were embedded in 12% gelatin (TAAB Laboratories) in PBS and solidified on ice for 15 min. Cell pellets were sectioned into cubes of 1 mm^3 and infiltrated at 4°C overnight with 2.1 M sucrose in PBS. Blocks were mounted on metal pins and frozen in liquid nitrogen. Ultrathin cryosections (50–100 nm) were prepared at −120°C with a diamond knife using an FC6 ultramicrotome (Leica Microsystems). Sections were collected into a mixture of 2% methylcellulose in H_2O and 2.1 M sucrose in PBS (1:1) and transferred after thawing to 200-mesh grids with a carbon-coated Formvar film.

Before labeling, grids were incubated in PBS at 37°C in a humid chamber for 25 min. Free aldehydes were quenched with 50 mM NH_4Cl (five times for 2 min each) before incubation with 1% BSA (once for 5 min). Cryosections were labeled with mouse rabbit VU219 anti-σ3 polyclonal antiserum, rabbit anti-LAMP-1 polyclonal antiserum (Abcam; ab24170), or both antisera diluted 1/50 in 1% BSA for 1 h. After washes with 0.1% BSA (five times for 2 min) and 1% BSA (once for 5 min), grids were incubated for 30 min with a secondary antibody conjugated with 5- or 10-nm colloidal gold particles (BB International) and diluted 1/100 in 1% BSA. Cryosections were washed with 0.1% BSA (two times for 2 min) and PBS (three times for 2 min) before post-fixation with 1% glutaraldehyde in PBS for 5 min. After washing with water (nine times for 2 min), grids were incubated with a mixture of uranyl acetate and methylcellulose (9:1) on ice for 5 min. Grids were partitioned individually from the methyl cellulose–uranyl acetate solution using a 3.5-mm-diameter wire loop. The excess of liquid from the loop was removed, and grids were allowed to dry. Images were acquired using a JEOL JEM 1400 Flash electron microscope operating at 120 kV equipped with a Gatan CMOS digital and direct detection camera.

ET and image processing

Thick sections (~300 nm) were collected on Quantifoil R3.5/1 Cu/Rh grids (Quantifol Micro Tools), incubated with 10 nm protein A-gold particles (Electron Microscopy Sciences) on one side of the section, and stained for 20 min with 2% uranyl acetate in water. Single- and dual-axis ET was conducted using a Tecnai G2 F20 transmission electron microscope (FEI) operated at 200 kV. Tilt series were collected automatically at 1.5° increments over an angular range of −60° to +60° with a nominal magnification of ×11,500 and pixel size of 1.01 nm. Images were recorded using an Eagle 4k×4k slow-scan charge-coupled device (FEI) using FEI software. Projection alignment and image processing was conducted using the IMOD program (Kremer et al., 1996). Visualization and final segmentation was conducted using Amira software. Before segmentation, some tomograms were subjected to "denoising" by a Gaussian filter application (Martinez-Sanchez et al., 2011, 2013, 2014). Eight tomograms showing different reovirus egress zones were recorded. The VI–SO–MC interface was analyzed from nine tomograms.

CLEM

HBMECs were cultured on grid photoetched coverslips (Electron Microscopy Sciences; 72265–25) and adsorbed with reovirus at an MOI of 1 PFU/cell. At 17 hpi, cells were incubated with 50 nM Lysotracker Red DND-99 (Invitrogen; L7528) for 1 h to label lysosomes. Cells were fixed using a mixture of 4% PFA and 0.1% glutaraldehyde in PBS for 1 h and imaged by phase-contrast and fluorescence microscopy using a Leica DMI6000B fluorescence microscope equipped with an HCX PL APO CS 20.0 × 0.70 dry UV objective and LAS X software. A total of 50 different zones were imaged, and infected cells with interesting features were selected for ultrastructural analysis. Cells were fixed with 4% PFA and 1% glutaraldehyde in PBS for 1 h and incubated with 1% osmium tetroxide and 0.8% potassium ferricyanide in water and 2% uranyl acetate. Samples were dehydrated in 5-min steps with increasing concentrations of ethanol (30%, 50%, 70%, 90%, and twice in 100%) at 4°C and embedded in EML-812 resin. Grid coverslips were separated from resin-embedded cells by immersion in liquid nitrogen. Ultrathin sections of selected cells were collected in 1% Formvar-coated GS2X1-C3 copper grids and stained with uranyl acetate and lead citrate. Ten cells were processed by serial sectioning and imaged with a JEOL JEM 1011 electron microscope operating at 100 kV equipped with a Gatan ES1000Ww digital camera.

Quantification and statistical analysis

Experiments were conducted with a minimum of three independent replicates. Data presented in the text are expressed as the mean ± SEM. Statistical significance was determined using two-sample unequal variance *t* test with two-tailed distribution

($\alpha = 0.05$). Graphs were prepared and statistical analyses were conducted using Microsoft Excel and Prism8 software.

Online supplemental material

Fig. S1 shows the attachment of mature virions to filaments and the LAMP-1 immunolabeling of thawed cryosections from uninfected and reovirus-infected cells. Fig. S2 shows the quantification of the number and size of LAMP-1–positive lysosomes in uninfected and reovirus-infected cells. Fig. S3 shows the pH of organelles of the endosomal–lysosomal pathway in uninfected and reovirus-infected cells as well as in lysosomes and SOs adjacent to VIs. Fig. S4 shows the reorganization of lysosomes and egress machinery in different cell lines and the confocal and electron micrographs of HBMECs infected with reovirus strains T1L and T3D. Fig. S5 shows the distribution of late and recycling endosomes during reovirus infection, immunofluorescence imaging of HeLa cells transfected with σ3-GFP and infected with reovirus, and confocal microscopy of cells infected with supernatants of transfected and infected cells. Video 1 shows a tomogram in 2D and 3D of a reovirus egress area. Video 2 shows a time-lapse recording of lysosomes in uninfected cells. Videos 3, 4, and 5 show time-lapse recordings of lysosomes in reovirus-infected cells. Video 6 shows a 3D model of LAMP-1 and reovirus σ1 in an infected cell. Videos 7 and 8 show TIRF microscopy of lysosomes and reovirus σ3-GFP in reovirus-infected cells. Video 9 shows TIRF microscopy of lysosomes in uninfected cells.

Acknowledgments

We thank members of the Risco and Dermody laboratories for many useful discussions. We are grateful to the UPMC Children's Hospital of Pittsburgh Rangos Research Center Cell Imaging Core Laboratory for assistance with microscopy. Special thanks to Dr. Martin Sachse for expert advice with Tokuyasu cryosections and high-pressure freezing and critical review of the manuscript, as well as Drs. Sylvia Gutiérrez-Erlandsson and Ana Oña for assistance with confocal microscopy. We thank Dr. Javier Chichón for assistance with ET.

This work was supported in part by Public Health Service awards AI032539 (T.S. Dermody and C. Risco), AI122563 (J.J. Knowlton), and GM007347 (J.J. Knowlton).

The authors declare no competing interests.

Author contributions: I. Fernández de Castro conceived, designed, and performed experiments; analyzed data; contributed materials and analysis tools; and wrote the paper. T.S. Dermody and C. Risco conceived and designed experiments, analyzed the data, contributed materials and analysis tools, and wrote the paper. R. Tenorio, P. Ortega-González, J.J. Knowlton, P.F. Zamora, and C.H. Lee conceived, designed, and performed experiments and analyzed data. J.J. Fernández conceived and designed experiments, analyzed data, and contributed materials and analysis tools. All authors reviewed, critiqued, and provided comments on the manuscript.

Submitted: 18 October 2019
Revised: 20 February 2020
Accepted: 6 April 2020

References

Altan-Bonnet, N.. 2017. Lipid Tales of Viral Replication and Transmission. *Trends Cell Biol.* 27:201–213. https://doi.org/10.1016/j.tcb.2016.09.011

Baer, G.S., and T.S. Dermody. 1997. Mutations in reovirus outer-capsid protein sigma3 selected during persistent infections of L cells confer resistance to protease inhibitor E64. *J. Virol.* 71:4921–4928. https://doi.org/10.1128/JVI.71.7.4921-4928.1997

Bär, S., L. Daeffler, J. Rommelaere, and J.P. Nüesch. 2008. Vesicular egress of non-enveloped lytic parvoviruses depends on gelsolin functioning. *PLoS Pathog.* 4. e1000126. https://doi.org/10.1371/journal.ppat.1000126

Bird, S.W., and K. Kirkegaard. 2015. Escape of non-enveloped virus from intact cells. *Virology*. 479–480:444–449. https://doi.org/10.1016/j.virol.2015.03.044

Bird, S.W., N.D. Maynard, M.W. Covert, and K. Kirkegaard. 2014. Nonlytic viral spread enhanced by autophagy components. *Proc. Natl. Acad. Sci. USA*. 111:13081–13086. https://doi.org/10.1073/pnas.1401437111

Bouziat, R., R. Hinterleitner, J.J. Brown, J.E. Stencel-Baerenwald, M. Ikizler, T. Mayassi, M. Meisel, S.M. Kim, V. Discepolo, A.J. Pruijssers, et al. 2017. Reovirus infection triggers inflammatory responses to dietary antigens and development of celiac disease. *Science*. 356:44–50. https://doi.org/10.1126/science.aah5298

Brandenburg, B., and X. Zhuang. 2007. Virus trafficking - learning from single-virus tracking. *Nat. Rev. Microbiol.* 5:197–208. https://doi.org/10.1038/nrmicro1615

Chen, Y.H., W. Du, M.C. Hagemeijer, P.M. Takvorian, C. Pau, A. Cali, C.A. Brantner, E.S. Stempinski, P.S. Connelly, H.C. Ma, et al. 2015. Phosphatidylserine vesicles enable efficient en bloc transmission of enteroviruses. *Cell*. 160:619–630. https://doi.org/10.1016/j.cell.2015.01.032

Chen, Y., Q. Chen, M. Li, Q. Mao, H. Chen, W. Wu, D. Jia, and T. Wei. 2017. Autophagy pathway induced by a plant virus facilitates viral spread and transmission by its insect vector. *PLoS Pathog.* 13. e1006727. https://doi.org/10.1371/journal.ppat.1006727

Christensen, K.A., J.T. Myers, and J.A. Swanson. 2002. pH-dependent regulation of lysosomal calcium in macrophages. *J. Cell Sci.* 115:599–607.

den Boon, J.A., A. Diaz, and P. Ahlquist. 2010. Cytoplasmic viral replication complexes. *Cell Host Microbe*. 8:77–85. https://doi.org/10.1016/j.chom.2010.06.010

Dermody, T.S., M.L. Nibert, J.D. Wetzel, X. Tong, and B.N. Fields. 1993. Cells and viruses with mutations affecting viral entry are selected during persistent infections of L cells with mammalian reoviruses. *J. Virol.* 67:2055–2063. https://doi.org/10.1128/JVI.67.4.2055-2063.1993

Ebert, D.H., J. Deussing, C. Peters, and T.S. Dermody. 2002. Cathepsin L and cathepsin B mediate reovirus disassembly in murine fibroblast cells. *J. Biol. Chem.* 277:24609–24617. https://doi.org/10.1074/jbc.M201107200

Elgner, F., H. Ren, R. Medvedev, D. Ploen, K. Himmelsbach, K. Boller, and E. Hildt. 2016. The Intracellular Cholesterol Transport Inhibitor U18666A Inhibits the Exosome-Dependent Release of Mature Hepatitis C Virus. *J. Virol.* 90:11181–11196. https://doi.org/10.1128/JVI.01053-16

Feng, Z., L. Hensley, K.L. McKnight, F. Hu, V. Madden, L. Ping, S.H. Jeong, C. Walker, R.E. Lanford, and S.M. Lemon. 2013. A pathogenic picornavirus acquires an envelope by hijacking cellular membranes. *Nature*. 496:367–371. https://doi.org/10.1038/nature12029

Fernández de Castro, I., P.F. Zamora, L. Ooms, J.J. Fernández, C.M. Lai, B.A. Mainou, T.S. Dermody, and C. Risco. 2014. Reovirus forms neo-organelles for progeny particle assembly within reorganized cell membranes. *MBio*. 5. e00931-13. https://doi.org/10.1128/mBio.00931-13

Fernández de Castro, I., R. Tenorio, and C. Risco. 2016. Virus assembly factories in a lipid world. *Curr. Opin. Virol.* 18:20–26. https://doi.org/10.1016/j.coviro.2016.02.009

Fontana, J., W.P. Tzeng, G. Calderita, A. Fraile-Ramos, T.K. Frey, and C. Risco. 2007. Novel replication complex architecture in rubella replicon-transfected cells. *Cell. Microbiol.* 9:875–890. https://doi.org/10.1111/j.1462-5822.2006.00837.x

Fontana, J., C. López-Iglesias, W.P. Tzeng, T.K. Frey, J.J. Fernández, and C. Risco. 2010. Three-dimensional structure of Rubella virus factories. *Virology*. 405:579–591. https://doi.org/10.1016/j.virol.2010.06.043

Frolova, E.I., R. Gorchakov, L. Pereboeva, S. Atasheva, and I. Frolov. 2010. Functional Sindbis virus replicative complexes are formed at the plasma membrane. *J. Virol.* 84:11679–11695. https://doi.org/10.1128/JVI.01441-10

Furlong, D.B., M.L. Nibert, and B.N. Fields. 1988. Sigma 1 protein of mammalian reoviruses extends from the surfaces of viral particles. *J. Virol.* 62:246–256. https://doi.org/10.1128/JVI.62.1.246-256.1988

Geisow, M.J.. 1984. Fluorescein conjugates as indicators of subcellular pH. A critical evaluation. *Exp. Cell Res.* 150:29–35. https://doi.org/10.1016/0014-4827(84)90698-0

Griffiths, G.M. 2016. Secretion from Myeloid Cells: Secretory Lysosomes. *Microbiol. Spectr.* 4:MCHD-0030-2016. https://doi.org/10.1128/microbiolspec.MCHD-0030-2016

Guglielmi, K.M., E.M. Johnson, T. Stehle, and T.S. Dermody. 2006. Attachment and cell entry of mammalian orthoreovirus. *Curr. Top. Microbiol. Immunol.* 309:1–38.

Hyatt, A.D., B.T. Eaton, and S.M. Brookes. 1989. The release of bluetongue virus from infected cells and their superinfection by progeny virus. *Virology*. 173:21–34. https://doi.org/10.1016/0042-6822(89)90218-3

Johnson, D.E., P. Ostrowski, V. Jaumouillé, and S. Grinstein. 2016. The position of lysosomes within the cell determines their luminal pH. *J. Cell Biol.* 212:677–692. https://doi.org/10.1083/jcb.201507112

Jourdan, N., J.P. Brunet, C. Sapin, A. Blais, J. Cotte-Laffitte, F. Forestier, A.M. Quero, G. Trugnan, and A.L. Servin. 1998. Rotavirus infection reduces sucrase-isomaltase expression in human intestinal epithelial cells by perturbing protein targeting and organization of microvillar cytoskeleton. *J. Virol.* 72:7228–7236. https://doi.org/10.1128/JVI.72.9.7228-7236.1998

Kar, A.K., N. Iwatani, and P. Roy. 2005. Assembly and intracellular localization of the bluetongue virus core protein VP3. *J. Virol.* 79:11487–11495. https://doi.org/10.1128/JVI.79.17.11487-11495.2005

Kemp, V., I.J.C. Dautzenberg, R.W. Limpens, D.J.M. van den Wollenberg, and R.C. Hoeben. 2017. Oncolytic Reovirus Infection Is Facilitated by the Autophagic Machinery. *Viruses*. 9:266.

Kirkbride, K.C., N.H. Hong, C.L. French, E.S. Clark, W.G. Jerome, and A.M. Weaver. 2012. Regulation of late endosomal/lysosomal maturation and trafficking by cortactin affects Golgi morphology. *Cytoskeleton (Hoboken)*. 69:625–643. https://doi.org/10.1002/cm.21051

Klionsky, D.J., E.L. Eskelinen, and V. Deretic. 2014. Autophagosomes, phagosomes, autolysosomes, phagolysosomes, autophagolysosomes... wait, I'm confused. *Autophagy*. 10:549–551. https://doi.org/10.4161/auto.28448

Kobayashi, T., A.A. Antar, K.W. Boehme, P. Danthi, E.A. Eby, K.M. Guglielmi, G.H. Holm, E.M. Johnson, M.S. Maginnis, S. Naik, et al. 2007. A plasmid-based reverse genetics system for animal double-stranded RNA viruses. *Cell Host Microbe*. 1:147–157. https://doi.org/10.1016/j.chom.2007.03.003

Kremer, J.R., D.N. Mastronarde, and J.R. McIntosh. 1996. Computer visualization of three-dimensional image data using IMOD. *J. Struct. Biol.* 116:71–76. https://doi.org/10.1006/jsbi.1996.0013

Lai, C.M., B.A. Mainou, K.S. Kim, and T.S. Dermody. 2013. Directional release of reovirus from the apical surface of polarized endothelial cells. *MBio*. 4:e00049-e13. https://doi.org/10.1128/mBio.00049-13

Lee, J.Y., J.A. Marshall, and D.S. Bowden. 1994. Characterization of rubella virus replication complexes using antibodies to double-stranded RNA. *Virology*. 200:307–312. https://doi.org/10.1006/viro.1994.1192

Maginnis, M.S., B.A. Mainou, A. Derdowski, E.M. Johnson, R. Zent, and T.S. Dermody. 2008. NPXY motifs in the beta1 integrin cytoplasmic tail are required for functional reovirus entry. *J. Virol.* 82:3181–3191. https://doi.org/10.1128/JVI.01612-07

Magliano, D., J.A. Marshall, D.S. Bowden, N. Vardaxis, J. Meanger, and J.Y. Lee. 1998. Rubella virus replication complexes are virus-modified lysosomes. *Virology*. 240:57–63. https://doi.org/10.1006/viro.1997.8906

Martinez-Sanchez, A., I. Garcia, and J.J. Fernandez. 2011. A differential structure approach to membrane segmentation in electron tomography. *J. Struct. Biol.* 175:372–383. https://doi.org/10.1016/j.jsb.2011.05.010

Martinez-Sanchez, A., I. Garcia, and J.J. Fernandez. 2013. A ridge-based framework for segmentation of 3D electron microscopy datasets. *J. Struct. Biol.* 181:61–70. https://doi.org/10.1016/j.jsb.2012.10.002

Martinez-Sanchez, A., I. Garcia, S. Asano, V. Lucic, and J.J. Fernandez. 2014. Robust membrane detection based on tensor voting for electron tomography. *J. Struct. Biol.* 186:49–61. https://doi.org/10.1016/j.jsb.2014.02.015

Maxfield, F.R.. 2014. Role of endosomes and lysosomes in human disease. *Cold Spring Harb. Perspect. Biol.* 6. a016931. https://doi.org/10.1101/cshperspect.a016931

Méndez, F., N. Romero, L.L. Cubas, L.R. Delgui, D. Rodríguez, and J.F. Rodríguez. 2017. Non-Lytic Egression of Infectious Bursal Disease Virus (IBDV) Particles from Infected Cells. *PLoS One*. 12. e0170080. https://doi.org/10.1371/journal.pone.0170080

Meo-Evoli, N., E. Almacellas, F.A. Massucci, A. Gentilella, S. Ambrosio, S.C. Kozma, G. Thomas, and A. Tauler. 2015. V-ATPase: a master effector of E2F1-mediated lysosomal trafficking, mTORC1 activation and autophagy. *Oncotarget*. 6:28057–28070. https://doi.org/10.18632/oncotarget.4812

Mindell, J.A.. 2012. Lysosomal acidification mechanisms. *Annu. Rev. Physiol.* 74:69–86. https://doi.org/10.1146/annurev-physiol-012110-142317

Miyazaki, N., A. Nakagawa, and K. Iwasaki. 2013. Life cycle of phytoreoviruses visualized by electron microscopy and tomography. *Front. Microbiol.* 4:306. https://doi.org/10.3389/fmicb.2013.00306

Münz, C.. 2017. The Autophagic Machinery in Viral Exocytosis. *Front. Microbiol.* 8:269. https://doi.org/10.3389/fmicb.2017.00269

Mutsafi, Y., and N. Altan-Bonnet. 2018. Enterovirus Transmission by Secretory Autophagy. *Viruses*. 10:10.

Nagashima, S., S. Jirintai, M. Takahashi, T. Kobayashi, T. Tanggis, T. Nishizawa, T. Kouki, Yashiro, and H. Okamoto. 2014. Hepatitis E virus egress depends on the exosomal pathway, with secretory exosomes derived from multivesicular bodies. *J. Gen. Virol.* 95:2166–2175. https://doi.org/10.1099/vir.0.066910-0

Ohkuma, S., and B. Poole. 1978. Fluorescence probe measurement of the intralysosomal pH in living cells and the perturbation of pH by various agents. *Proc. Natl. Acad. Sci. USA*. 75:3327–3331. https://doi.org/10.1073/pnas.75.7.3327

Parker, J.S., T.J. Broering, J. Kim, D.E. Higgins, and M.L. Nibert. 2002. Reovirus core protein mu2 determines the filamentous morphology of viral inclusion bodies by interacting with and stabilizing microtubules. *J. Virol.* 76:4483–4496. https://doi.org/10.1128/JVI.76.9.4483-4496.2002

Perlman, M., and M.D. Resh. 2006. Identification of an intracellular trafficking and assembly pathway for HIV-1 gag. *Traffic*. 7:731–745. https://doi.org/10.1111/j.1398-9219.2006.00428.x

Rodríguez, A., P. Webster, J. Ortego, and N.W. Andrews. 1997. Lysosomes behave as Ca2+-regulated exocytic vesicles in fibroblasts and epithelial cells. *J. Cell Biol.* 137:93–104. https://doi.org/10.1083/jcb.137.1.93

Roy, D., D.R. Liston, V.J. Idone, A. Di, D.J. Nelson, C. Pujol, J.B. Bliska, S. Chakrabarti, and N.W. Andrews. 2004. A process for controlling intracellular bacterial infections induced by membrane injury. *Science*. 304:1515–1518. https://doi.org/10.1126/science.1098371

Salzman, N.H., and F.R. Maxfield. 1988. Intracellular fusion of sequentially formed endocytic compartments. *J. Cell Biol.* 106:1083–1091. https://doi.org/10.1083/jcb.106.4.1083

Schindelin, J., I. Arganda-Carreras, E. Frise, V. Kaynig, M. Longair, T. Pietzsch, S. Preibisch, C. Rueden, S. Saalfeld, B. Schmid, et al. 2012. Fiji: an open-source platform for biological-image analysis. *Nat. Methods*. 9:676–682. https://doi.org/10.1038/nmeth.2019

Seguin, S.J., F.F. Morelli, J. Vinet, D. Amore, S. De Biasi, A. Poletti, D.C. Rubinsztein, and S. Carra. 2014. Inhibition of autophagy, lysosome and VCP function impairs stress granule assembly. *Cell Death Differ.* 21:1838–1851. https://doi.org/10.1038/cdd.2014.103

Settembre, C., A. Fraldi, D.L. Medina, and A. Ballabio. 2013. Signals from the lysosome: a control centre for cellular clearance and energy metabolism. *Nat. Rev. Mol. Cell Biol.* 14:283–296. https://doi.org/10.1038/nrm3565

Spuul, P., G. Balistreri, L. Kääriäinen, and T. Ahola. 2010. Phosphatidylinositol 3-kinase-, actin-, and microtubule-dependent transport of Semliki Forest Virus replication complexes from the plasma membrane to modified lysosomes. *J. Virol.* 84:7543–7557. https://doi.org/10.1128/JVI.00477-10

Sturzenbecker, L.J., M. Nibert, D. Furlong, and B.N. Fields. 1987. Intracellular digestion of reovirus particles requires a low pH and is an essential step in the viral infectious cycle. *J. Virol.* 61:2351–2361. https://doi.org/10.1128/JVI.61.8.2351-2361.1987

Tenorio, R., I. Fernández de Castro, J.J. Knowlton, P.F. Zamora, C.H. Lee, B.A. Mainou, T.S. Dermody, and C. Risco. 2018. Reovirus σNS and μNS Proteins Remodel the Endoplasmic Reticulum to Build Replication Neo-Organelles. *MBio*. 9. e01253-18. https://doi.org/10.1128/mBio.01253-18

Thete, D., and P. Danthi. 2015. Conformational changes required for reovirus cell entry are sensitive to pH. *Virology*. 483:291–301. https://doi.org/10.1016/j.virol.2015.04.025

Tinevez, J.Y., N. Perry, J. Schindelin, G.M. Hoopes, G.D. Reynolds, E. Laplantine, S.Y. Bednarek, S.L. Shorte, and K.W. Eliceiri. 2017. TrackMate: An open and extensible platform for single-particle tracking. *Methods*. 115:80–90. https://doi.org/10.1016/j.ymeth.2016.09.016

Traub, L.M., S.I. Bannykh, J.E. Rodel, M. Aridor, W.E. Balch, and S. Kornfeld. 1996. AP-2-containing clathrin coats assemble on mature lysosomes. *J. Cell Biol.* 135:1801–1814. https://doi.org/10.1083/jcb.135.6.1801

Trejo-Cerro, O., C. Eichwald, E.M. Schraner, D. Silva-Ayala, S. Lopez, and C.F. Arias. 2017. Actin-dependent non-lytic rotavirus exit and infectious virus morphogenetic pathway in non-polarized cells. *J. Virol.* 92. e02076-17. https://doi.org/10.1128/JVI.02076-17

Virgin, H.W.T., IV, M.A. Mann, B.N. Fields, and K.L. Tyler. 1991. Monoclonal antibodies to reovirus reveal structure/function relationships between capsid proteins and genetics of susceptibility to antibody action. *J. Virol.* 65:6772–6781. https://doi.org/10.1128/JVI.65.12.6772-6781.1991

Wilhelm, L.P., C. Wendling, B. Védie, T. Kobayashi, M.P. Chenard, C. Tomasetto, G. Drin, and F. Alpy. 2017. STARD3 mediates endoplasmic reticulum-to-endosome cholesterol transport at membrane contact sites. *EMBO J.* 36:1412–1433. https://doi.org/10.15252/embj.201695917

Xu, H., and D. Ren. 2015. Lysosomal physiology. *Annu. Rev. Physiol.* 77:57–80. https://doi.org/10.1146/annurev-physiol-021014-071649

JCB

Supplemental material

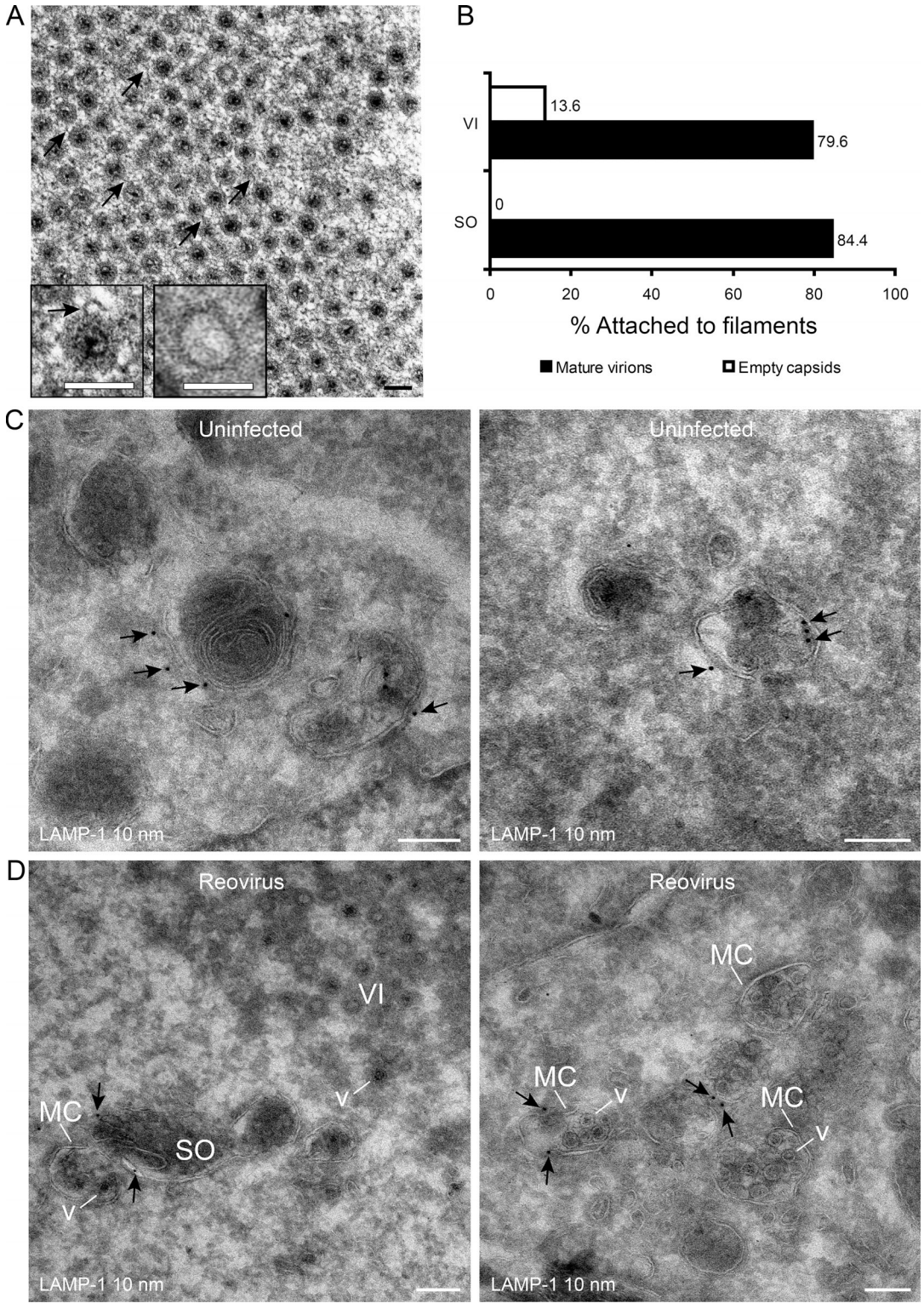

Figure S1. **Mature virions are attached to filaments inside reovirus inclusion and immunogold labeling of LAMP-1 in uninfected and reovirus-infected HBMECs. (A and B)** HBMECs were adsorbed with reovirus T1L M1-P208S at an MOI of 1 PFU/cell and processed at 18 hpi by high-pressure freezing, freeze substitution, ultra-thin sectioning, and TEM. **(A)** High-magnification view of a VI showing virions and filaments (arrows). The inset on the left shows a mature virion attached to a filament (arrow). The inset on the right shows an empty viral particle with no filaments. **(B)** The histogram depicts quantification of mature virions and empty viral particles attached to filaments in VIs and SOs as detected by TEM of infected cells. A total of 889 virions and 117 empty capsids in VIs and 332 virions in SOs were included in the quantification. Scale bars, 100 nm for main field, 80 nm for insets. **(C and D)** HBMECs were adsorbed with reovirus T1L M1-P208S at an MOI of 1 PFU/cell and cryosectioned using the Tokuyasu method at 18 hpi. Sections were immunogold labeled for LAMP-1 using secondary antibodies conjugated with 10-nm gold particles. **(C)** Lysosome-like structures labeled for LAMP-1 (arrows) in uninfected cells. **(D)** In reovirus-infected cells, LAMP-1 labeling was apparent in the membrane of SOs and MCs (arrows) adjacent to VIs. V, virion. Scale bars, 200 nm.

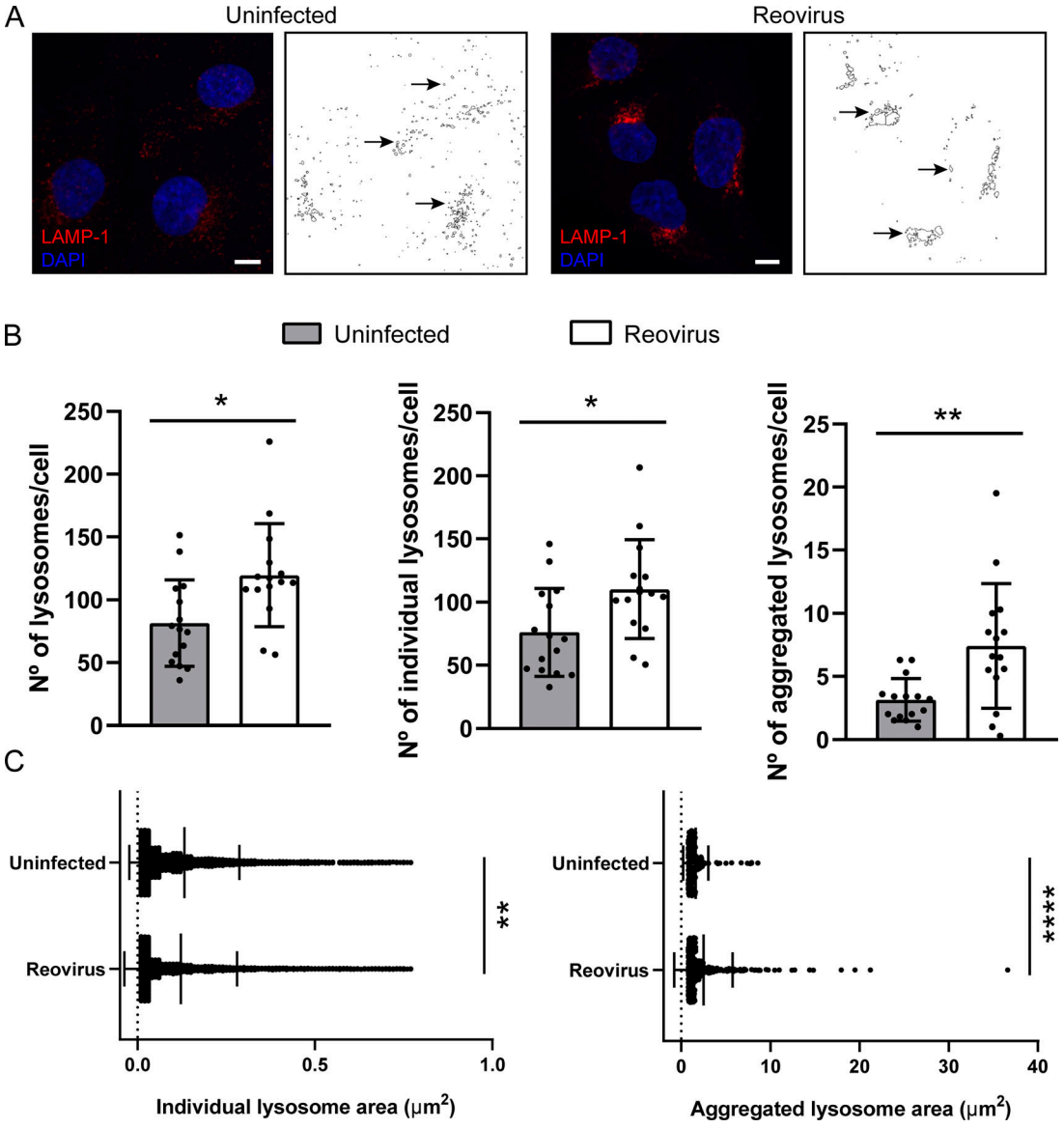

Figure S2. **Quantification of the number and size of lysosomes in uninfected and reovirus-infected cells.** HBMECs were adsorbed with reovirus T3D at an MOI of 1 PFU/cell. At 18 hpi, cells were fixed and processed for immunofluorescence and confocal microscopy. **(A)** Representative immunofluorescence images of cells labeled with antibodies specific for LAMP-1 (red) in uninfected and reovirus-infected cells. Nuclei are labeled with DAPI (blue). Lysosome number and size were quantified using ImageJ-Fiji software. Segmented images of confocal data with lysosome areas labeled with LAMP-1 are shown (arrows). Scale bars, 10 µm. **(B)** Quantification of total, individual, and aggregated LAMP-1–positive lysosomes per cell in uninfected and reovirus-infected cells. An area of <0.78 µm^2 corresponds to individual lysosomes; areas of ≥0.78 µm^2 are defined as aggregated lysosomes. The results are presented as mean ± SEM. Each data point represents the number of total, individual, and aggregated lysosomes, respectively, in a cell (n = 52 cells pooled from three independent experiments; *, P < 0.05; **, P < 0.01, unpaired two-tailed Student's t test). **(C)** Quantification of individual and aggregated lysosome size in uninfected and reovirus-infected cells. Each data point represents the lysosome size quantified with ImageJ-Fiji software (n = 52 cells pooled from three independent experiments; **, P < 0.01; ****, P < 0.0001, unpaired two-tailed Student's t test).

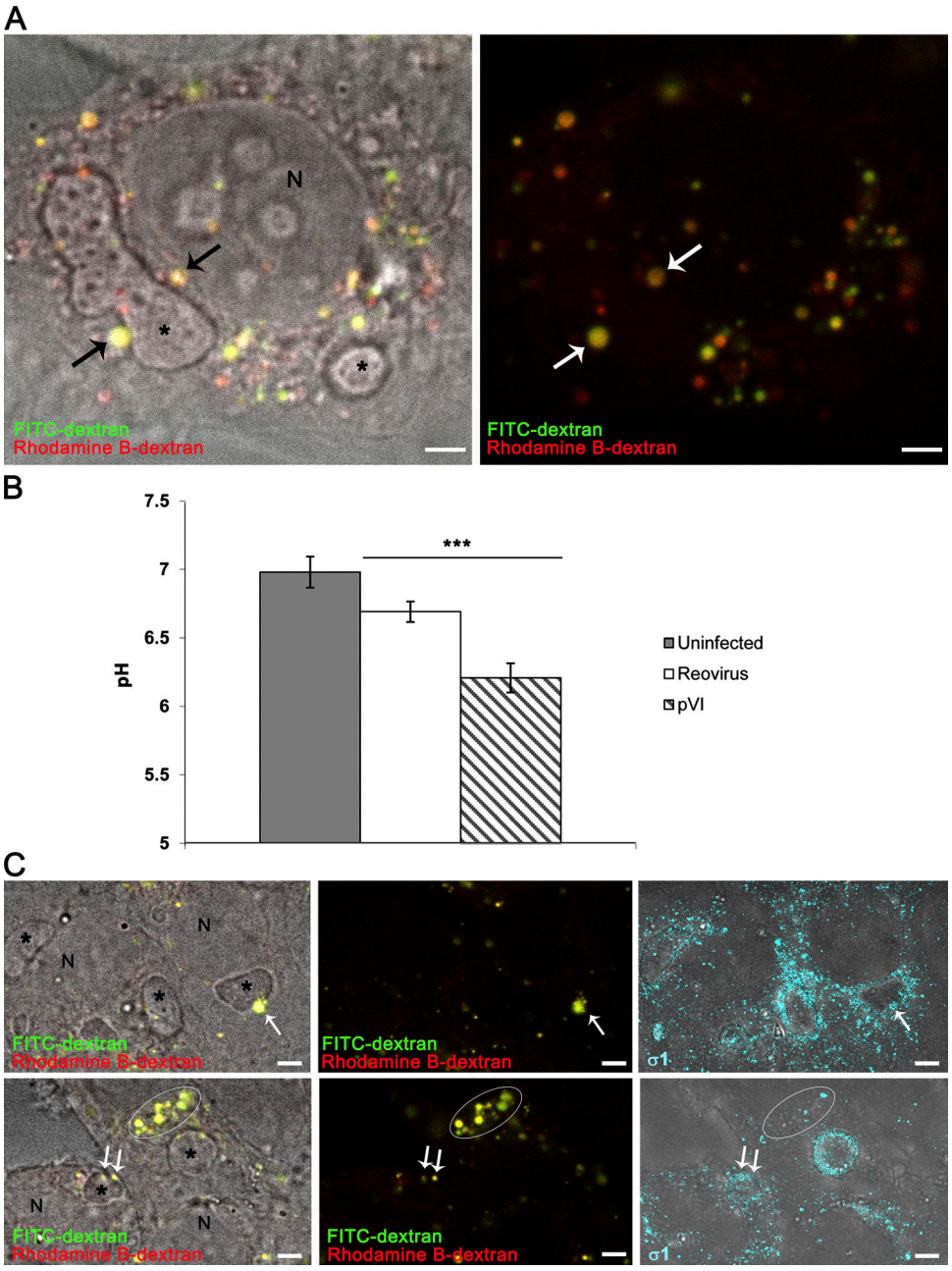

Figure S3. **pH of organelles of the endosomal-lysosomal compartment.** HBMECs were either mock-infected or adsorbed with reovirus T3D at an MOI of 1 PFU/cell, incubated for 4 h, and then incubated for an additional 16 h with FITC- and rhodamine–dextran probes. **(A)** Phase-contrast image and confocal single optical sections of an infected cell showing compartments labeled with FITC (green, more neutral) and rhodamine (red, more acidic) probes. Arrows indicate yellow lysosome-like organelles that contain both FITC and rhodamine probes adjacent to a VI (asterisk) as an example of pVI organelles included in the pVI quantification. **(B)** Results are presented as median ± SEM of three independent experiments. The median pH values of endosomal–lysosomal compartments in uninfected and reovirus-infected cells are 6.98 and 6.69, respectively. The pH of organelles adjacent to VIs (pVI) is 6.1. This value differs significantly from the pH of the endosomal–lysosomal compartment in infected cells (***, $P < 0.001$, unpaired two-tailed Student's *t* test). **(C)** Phase-contrast images and confocal single optical sections of four infected cells showing yellow lysosome-like organelles (arrows) adjacent to VIs (asterisks). The white ellipse surrounds a group of these organelles. Images on the right show the same cells after immunofluorescence with anti-σ1 antibody. Lysosome-like organelles, either with or without virions contained within, have the same color and a pH of ∼6.1. N, nucleus. Scale bars, 3 µm.

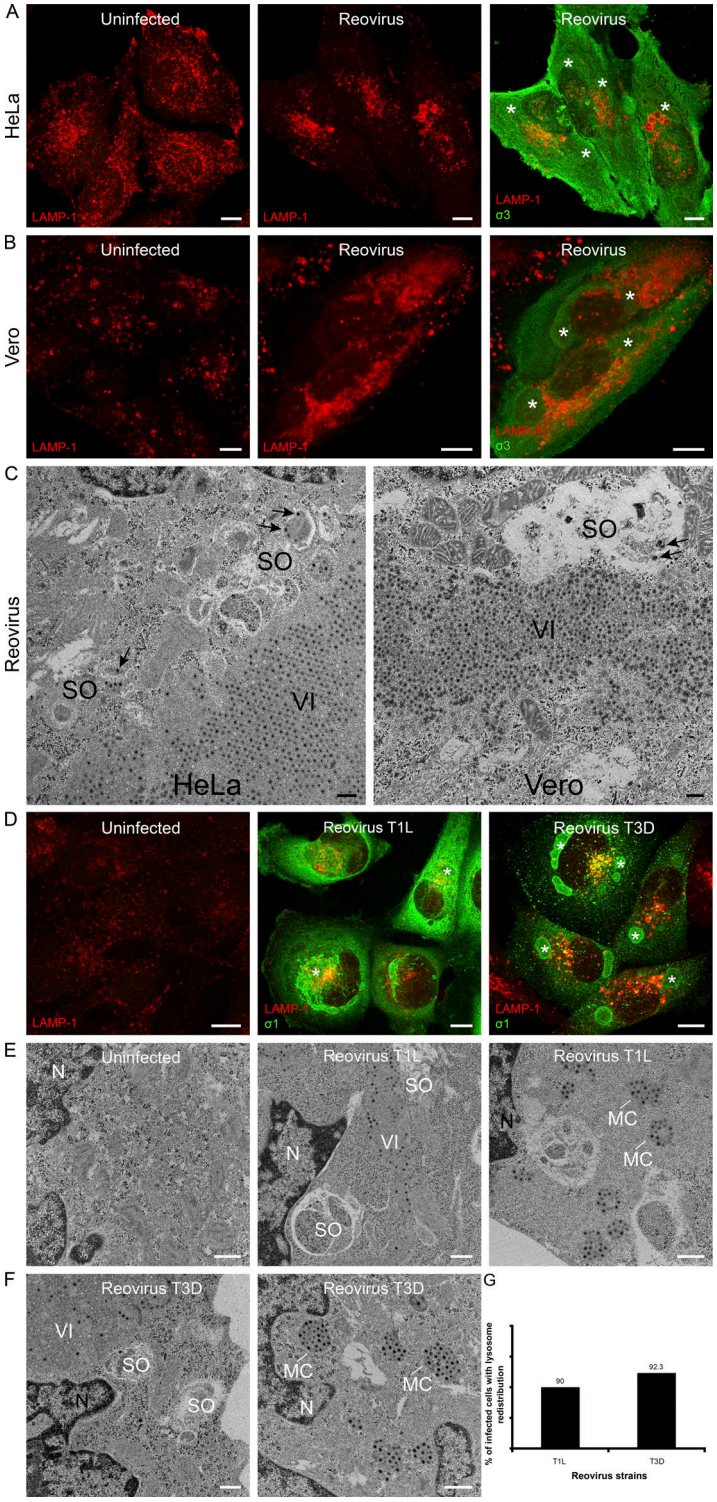

Figure S4. **Redistribution of lysosomes during reovirus infection in other cell lines and in HBMECs infected by other reovirus strains. (A–C)** HeLa cells and Vero cells were adsorbed with reovirus T1L M1-P208S at MOIs of 1 and 5 PFUs/cell, respectively. At 18 hpi, cells were fixed and processed for confocal microscopy and EM. **(A and B)** Immunofluorescence images of uninfected and reovirus-infected cells stained with antibodies specific for LAMP-1 (red) and σ3 (rabbit VU219, green). Lysosomes are recruited to VIs (asterisks) in reovirus-infected HeLa cells and Vero cells. Scale bars, 10 µm. **(C)** EM images showing VIs surrounded by SOs containing virions (arrows). Scale bars, 200 nm. **(D–G)** HBMECs were adsorbed with reovirus strains T1L and T3D at an MOI of 1 PFU/cell. At 18 hpi, cells were fixed and processed for fluorescence and EM. **(D)** Confocal images of uninfected and reovirus-infected cells labeled with antibodies specific for LAMP-1 (red) and reovirus σ1 protein (mouse monoclonal antibody 5C6 specific for T1L σ1 and mouse monoclonal antibody 9GB5 specific for T3D σ1, green). Lysosomes reorganize adjacent to VIs (asterisks) during reovirus T1L and T3D infection. Scale bars, 10 µm. **(E and F)** TEM images showing uninfected and reovirus T1L- and T3D-infected cells. SOs and MCs are observed adjacent to VIs in infected cells. N, nucleus. Scale bars, 500 nm. **(G)** Quantification of lysosome redistribution around inclusions as detected by confocal microscopy of infected cells.

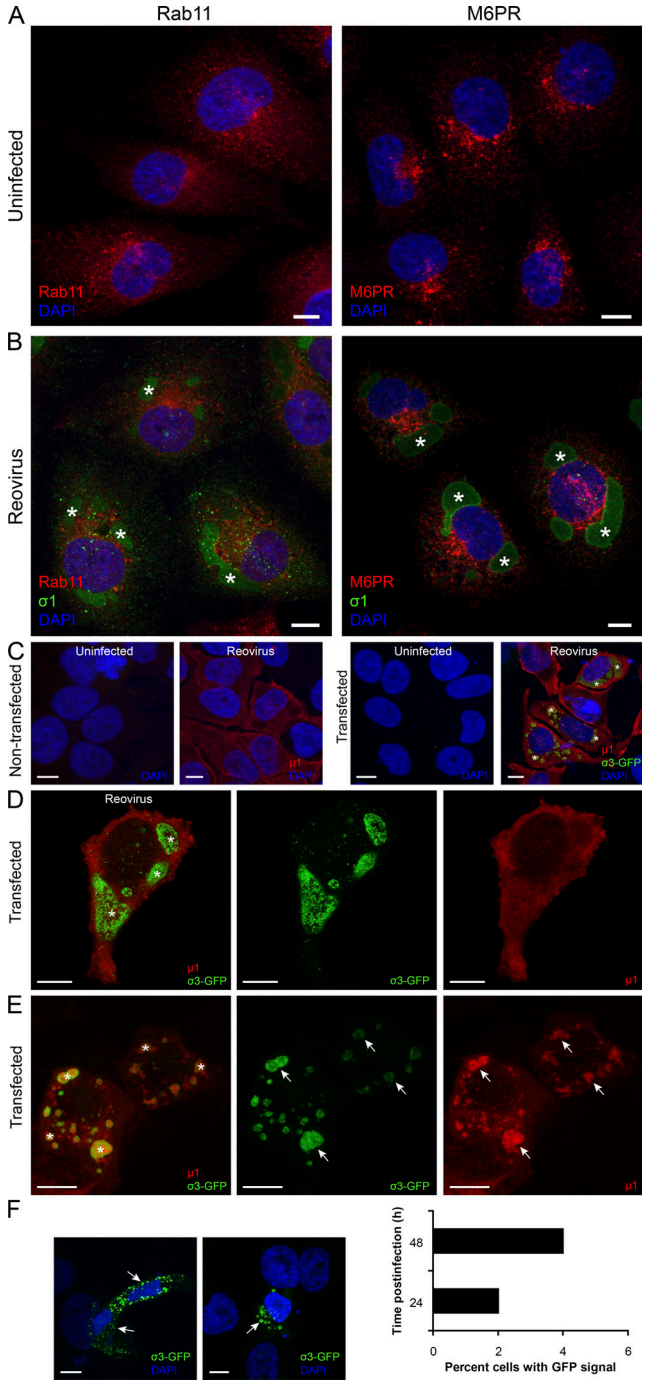

Figure S5. **Distribution of endosomes in reovirus-infected HBMECs and release of fluorescent, infectious viruses from HeLa cells transfected with a σ3-GFP plasmid and infected with reovirus.** HBMECs were either mock infected or adsorbed with reovirus T3D at an MOI of 1 PFU/cell and processed at 18 hpi for confocal microscopy. **(A and B)** Immunofluorescence images of uninfected and reovirus-infected cells stained with antibodies specific for markers of recycling and late endosomes, Rab11 and M6PR, respectively (red), and the reovirus σ1 protein (mouse monoclonal antibody 9GB5 specific for T3D σ1, green). Nuclei are labeled with DAPI (blue). Rab11- and M6PR-positive endosomes distribute throughout the cytosol in uninfected and reovirus-infected cells without clustering close to or within inclusions (asterisks). The M6PR-positive endosome signal concentrates in the perinuclear region of uninfected and reovirus-infected cells. Scale bars, 10 μm. **(C–E)** HeLa cells were transfected with a σ3-GFP plasmid for 24 h and adsorbed with reovirus T1L M1-P208S at an MOI of 10 PFUs/cell. Cells were fixed at 16, 24, and 48 hpi and stained using immunofluorescence. Confocal images of uninfected and reovirus-infected cells after transfection and stained with an antibody specific for the reovirus outer-capsid protein μ1 (mouse 8H6, red). Nuclei are labeled with DAPI (blue), and σ3 is visualized by virtue of its GFP fusion protein (green). The σ3-GFP signal concentrates in VIs (asterisks), as shown in three representative examples (C [fourth panel], D, and E). The σ3-GFP signal has the same distribution pattern as the reovirus μ1 outer-capsid protein (arrows in E, panels on the right). Scale bars, 10 μm. **(F)** HeLa cells were adsorbed with supernatants from σ3-GFP transfected and reovirus-infected cells collected at 24 and 48 hpi, fixed at 1.5 hpi, and processed for confocal microscopy. The left panels show representative fluorescence images of cells containing a σ3-GFP signal (arrows, green). Nuclei are stained with DAPI (blue). Quantification of the percentage of HeLa cells with GFP signal after infection with supernatants of cells transfected with σ3-GFP plasmid and infected with reovirus 24 or 48 hpi. Scale bars, 500 nm.

Video 1. **3D model of a reovirus egress zone visualized by ET (related to Fig. 2).** The 3D model was constructed using e-tomo and a combination of masking, isosurface, and manual tracing with Amira segmentation tools. Black spots represent gold particles used as fiducials. The computational slices of the tomogram are first swept upwards (first third of the video) and then backward (second third), revealing the 3D isosurface representation. The last third of the video rotates the 3D representation showing the MC on the cytosolic side and extracellular virions facing channels in the plasma membrane. The speed of the video is 24 frames per second. MC, gold; membranous channels, beige; viral particles, blue; plasma membrane, green; filaments, pink.

Video 2. **Live-cell microscopy showing lysosome movement in mock-infected cells.** Uninfected HBMECs were labeled with LysoTracker (red). Fluorescence and phase-contrast images were collected every 30 min for 24 h using a 40× objective. The speed of this video is 3 frames per second. Lysosomes showed uniform movement in the cytoplasm and mostly concentrate around the nucleus.

Video 3. **Live-cell microscopy showing lysosome movement in reovirus-infected cells.** HBMECs were adsorbed with reovirus T1L M1-P208S at an MOI of 1 PFU/cell and labeled with LysoTracker (red) at 1 hpi. Fluorescence and phase-contrast images were collected every 30 min for 24 h using a 40× objective. The speed of this video is 2 frames per second. VIs are dense, globular structures as detected by phase-contrast microscopy. SOs labeled with LysoTracker are dynamic structures that move along cytoskeletal filaments around VIs.

Video 4. **High-magnification, live-cell microscopy of lysosome movement in reovirus-infected cells.** HBMECs were adsorbed with reovirus T1L M1-P208S at an MOI of 1 PFU/cell and labeled with LysoTracker (red) at 1 hpi. Fluorescence and phase-contrast images were collected every 30 min for 3 h using a 63× objective. Speed, 1 frame per second. Lysosomes recruited to VIs fuse to form larger structures (red arrows).

Video 5. **High-magnification, live-cell microscopy of lysosome movements in reovirus-infected cells.** HBMECs were adsorbed with reovirus T1L M1-P208S at an MOI of 1 PFU/cell and labeled with LysoTracker (red) at 1 hpi. Fluorescence and phase-contrast images were collected every 30 min for 3 h using a 63× objective. Speed, 1 frame per second. In reovirus-infected cells, smaller MC-like vesicles labeled with LysoTracker (marked with red arrows) detach from the region with lysosomes, SOs, and VIs (arrows) and move to the cell periphery.

Video 6. **3D reconstruction of lysosome recruitment in reovirus-infected cells (related to Fig. 5).** HBMECs were adsorbed with reovirus T3D at an MOI of 1 PFU/cell and processed at 18 hpi for immunofluorescence and confocal microscopy. Lysosomes were stained using antibodies specific for LAMP-1 (red) and reovirus σ1 capsid protein (mouse monoclonal antibody 9GB5, green). Images were processed using ImageJ-Fiji and Imaris software. This video shows the 3D reconstruction of an image stack in which the red and green isosurfaces correspond to LAMP-1 and σ1 signals, respectively. Speed, 5 frames per second. There are discrete areas close to the inclusions (observed as perinuclear green structures) in which both signals accumulate.

Video 7. **Superresolution live-cell microscopy of lysosome dynamics in reovirus-infected cells (related to Fig. 7).** HeLa cells were transfected with a σ3-GFP plasmid for 24 h and adsorbed with reovirus T1L M1-P208S at an MOI of 10 PFUs/cell for 1 h. At 16 hpi, cells were imaged every 3 s for 30 min using TIRF microscopy to visualize basal reovirus egress zones. Speed, 3 frames per second. The TIRF microscopy movie shows lysosomes stained with LysoTracker (red) and σ3 visualized with the GFP fusion protein (green). Reovirus σ3 concentrates in lysosomes and moves to the cell periphery. In this infected cell, there are two reovirus egress areas in which both lysosome and σ3 signals intensify.

Video 8. **Superresolution live-cell microscopy of lysosome dynamics in reovirus-infected cells.** HeLa cells were transfected with a σ3-GFP plasmid for 24 h and adsorbed with reovirus T1L M1-P208S at an MOI of 10 PFUs/cell for 1 h. At 16 hpi, cells were imaged every 3 s for 30 min using TIRF microscopy to visualize basal reovirus egress zones. Speed, 3 frames per second. The TIRF microscopy movie shows lysosomes stained with LysoTracker (red) and σ3 visualized with the GFP fusion protein (green). This is a higher magnification of a reovirus egress zone in which both lysosome and reovirus σ3 signals accumulate.

Video 9. **Superresolution live-cell microscopy of lysosomes in uninfected cells.** HeLa cells were incubated with LysoTracker for 30 min and imaged using TIRF microscopy to visualize lysosome movements at the basal surface. Speed, 3 frames per second. Lysosomes (red) move randomly throughout the cell base.